

AD-A108 408 NAVAL RESEARCH LAB WASHINGTON DC
MULTIPATH VLF PROPAGATION EFFECTS ON COM
SEP 81 F J KELLY, J P MAUSER, M M BECK
UNCLASSIFIED NRL-8521

NAVAL RESEARCH LAB WASHINGTON DC

MULTIPATH VLF PROPAGATION EFFECTS ON CORRELATION RECEIVERS, (U)

SEP 81 F J KELLY, J P HAUSER, H M BECK

F/G 20/14

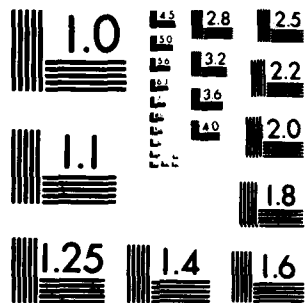
UNCLASSIFIED

NRL-8521

NL

100

END
DATE
FILMED
1 82
DTIC



MICROCOPY RESOLUTION TEST CHART
NATIONAL BUREAU OF STANDARDS 1963-A₁

AD A108408


NRL Report 8521

LEVEL II

Multipath VLF Propagation Effects on Correlation Receivers

F. J. KELLY

*E.O. Hulburt Center for Space Research
Ionospheric Effects Branch
Space Sciences Division*

and

J. P. HAUSER, H. M. BECK, AND F. J. RHOADS

*Information Technology
Communication Sciences Division*

September 18, 1981



**DTIC
ELECTE
DEC 11 1981**
S D D

NAVAL RESEARCH LABORATORY
Washington, D.C.

Approved for public release; distribution unlimited.

81 12 10 061

DTIC FILE COPY

REPORT DOCUMENTATION PAGE		READ INSTRUCTIONS BEFORE COMPLETING FORM	
1. REPORT NUMBER NRL Report 8521	2. GOVT ACCESSION NO. AD-A208408	3. RECIPIENT'S CATALOG NUMBER	
4. TITLE (and Subtitle) MULTIPATH VLF PROPAGATION EFFECTS ON CORRELATION RECEIVERS		5. TYPE OF REPORT & PERIOD COVERED	
		6. PERFORMING ORG. REPORT NUMBER	
7. AUTHOR(s) Francis J. Kelly, J.P. Hauser, H.M. Beck, and F.J. Rhoads		8. CONTRACT OR GRANT NUMBER(s)	
9. PERFORMING ORGANIZATION NAME AND ADDRESS Naval Research Laboratory Washington, DC 20375		10. PROGRAM ELEMENT, PROJECT, TASK AREA & WORK UNIT NUMBERS	
11. CONTROLLING OFFICE NAME AND ADDRESS		12. REPORT DATE September 18, 1981	
		13. NUMBER OF PAGES 51	
14. MONITORING AGENCY NAME & ADDRESS (if different from Controlling Office) Naval Electronics Systems Command Washington, DC 20360		15. SECURITY CLASS. (of this report) UNCLASSIFIED	
		15a. DECLASSIFICATION/DOWNGRADING SCHEDULE	
16. DISTRIBUTION STATEMENT (of this Report) Approved for public release; distribution unlimited.			
17. DISTRIBUTION STATEMENT (of the abstract entered in Block 20, if different from Report)			
18. SUPPLEMENTARY NOTES			
19. KEY WORDS (Continue on reverse side if necessary and identify by block number) VLF propagation Multipath Earth-ionosphere waveguide Correlation Minimum shift keying Waveform distortion			
20. ABSTRACT (Continue on reverse side if necessary and identify by block number) The effect of electromagnetic propagation at very low frequency in the earth ionosphere waveguide can distort wideband communication waveforms and produce a splitting of the correlation peak of the received signal at a model interference null where multipath signals arrive out of phase. Propagation from an inclined dipole antenna trailed behind an orbiting aircraft can cause split correlation pattern to fluctuate throughout the orbit period. For the case of an MSK (minimum-shift-keying) signal format, expressions and graphs are given for the correlation vector, as a function of receiver synchronization time and aircraft flight direction.			

SECURITY CLASSIFICATION OF THIS PAGE (When Data Entered)

257950 sk

CONTENTS

INTRODUCTION	1
THEORY	3
Elementary Signal Theory	3
Modulation Methods	6
MSK Signals	6
THE MSK CORRELATION RECEIVER	7
TWO PROPAGATION MODES AND A STATIONARY TRANSMITTER	10
FIELD-STRENGTH EXPRESSIONS	10
CORRELATION EFFECTS OF ANTENNA ROTATION	11
DIAGRAMMATIC REPRESENTATIONS	13
NUMERICAL CALCULATIONS	19
Procedures	19
Results	21
Discussion	48
CONCLUSIONS	49
REFERENCES	49

Accession For	
NTIS GRA&I	<input checked="" type="checkbox"/>
DTIC TAB	<input type="checkbox"/>
Unannounced	<input type="checkbox"/>
Justification	
By _____	
Distribution/	
Availability Codes	
Dist	Avail and/or Special
A	

S DTIC
 ELECTE D
 DEC 11 1981
 D

MULTIPATH VLF PROPAGATION EFFECTS ON CORRELATION RECEIVERS

INTRODUCTION

The propagation of very-low frequency (VLF) waves over terrestrial paths is often treated by considering the space between the earth and the ionosphere to be the interior of a waveguide, with the earth as a lower boundary and the D and E layers of the ionosphere as an upper boundary. Ordinarily several waveguide modes can propagate with low attenuation in the guide. Where two modes have approximately equal strength and arrive with approximately 180° phase shift between their wave components, a modal interference null is said to occur. Typical examples of such modal interference nulls are shown in Fig. 1, taken from Rhoads and Garner [1]. The predicted curves for Fig. 1 were those generated using the theoretical waveguide formulation of Wait and Spies [2].

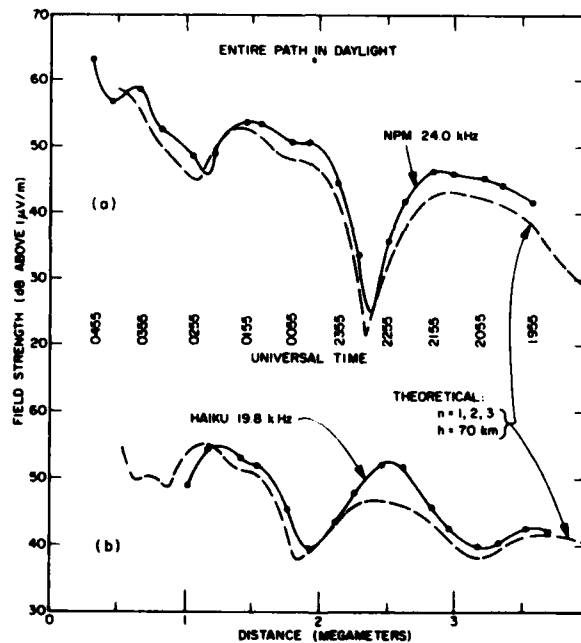


Fig. 1 — Comparison of theoretical results from Wait and Spies [2] with observed records in flight from San Francisco to Honolulu, May 18-19, 1965, for radiated power $P_r = 1$ kW

When an airborne facility transmits VLF waves using a trailing-wire antenna, a complicated time-varying field is produced at a receiver [3,4]. The inclined antenna can be considered a superposition of an elevated vertical and horizontal antenna. Both quasi-transverse magnetic and electric modes are generated by the inclined antenna. The amplitudes of these modes vary with the angle between the horizontal component of the antenna and the direction to the receiver. If the horizontally and vertically

Manuscript submitted August 6, 1981.

generated resultant fields are nearly equal in magnitude at a receiver location, rather deep oscillations in the received field strength may occur during the period of an orbit. These oscillations often occur during nighttime propagation conditions but can occur during daytime also. Figure 2 shows the signal reception pattern versus distance and time for an airborne transmitting facility flying in good orbit (verticality $\approx 70\%$) during daytime. Figure 3 shows the same pattern for a poor orbit (verticality $\approx 10\%$) during nighttime. The observed fluctuations range from mild to extreme.

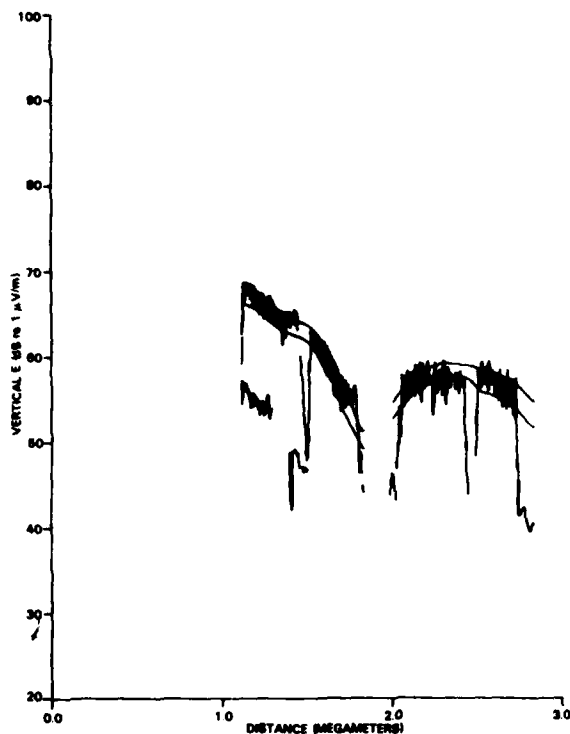


Fig. 2 — Field strength versus distance measured during daylight hours on an aircraft flying radially toward an airborne broadcasting facility in good orbit near Jacksonville, Florida on March 27, 1971, with the frequency being 19.4 kHz

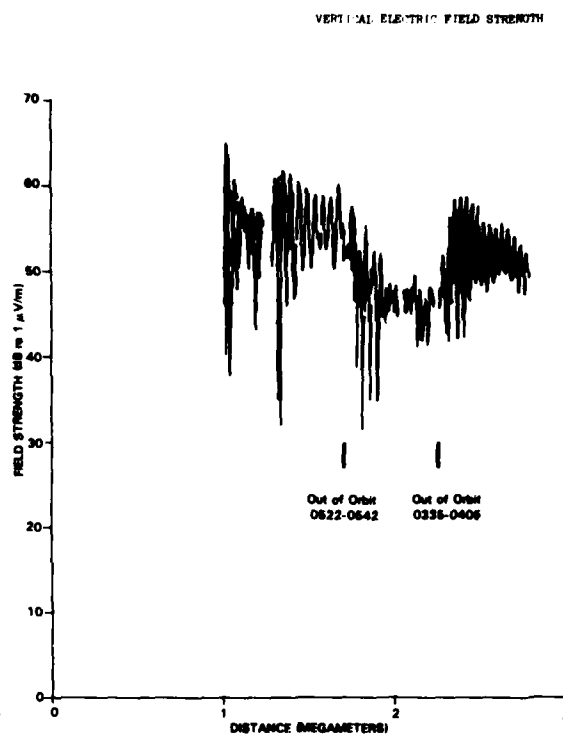


Fig. 3 — Field strength versus distance measured during nighttime hours on aircraft flying radially toward airborne broadcasting facility in poor orbit near Jacksonville, Florida on April 5, 1971, with the frequency being 25.6 kHz

An important task of airborne VLF facilities is to broadcast wideband spread-spectrum VLF communication signals. These signals may be distorted by the propagation through the waveguide and by the variation in aircraft direction in orbit. To determine the deleterious results caused by these circumstances, it is necessary to examine the correlation of the received signal with an exact replica of the transmitted waveform to estimate the effective signal reduction.

A study of correlation receiver distortion due to propagation effects was performed by Rothmuller [5] for the case of broadcast from a fixed transmitter to a fixed receiver. Rothmuller showed that when two multipath signals interfere at a point, two correlation peaks occur separated in receiver synchronization time τ_R by approximately the duration of a spread-spectrum signaling element (chip). The maximum value of the correlation could be on the earlier or later correlation peak. In the present report we go a step further by including the effects of aircraft orbit on correlation receiver signal output. We study the condition of a time-varying wideband multipath situation common in airborne facility usage by considering the case in which the signaling elements (chips) are minimum-shift-keying (MSK)

waveforms and the communication decision is based on the coherent integration of a series of such waveforms.

In some circumstances the performance of the correlators depends greatly on which instant within a chip the correlator is synchronized to. It appears probable that a bit decision based on several correlations within a chip period would be superior to a decision based on a single correlation within a chip.

THEORY

Elementary Signal Theory

Figure 4 shows schematically the outlines of the communication system under discussion. Figure 5 shows a conceptual version of a receiver and demodulation portion of Fig. 4. The operation of the integrator portion of the equipment in Fig. 5 is to sample the received waveforms $h(t)$ and to multiply them by the desired waveform $h_1(t)$ and $h_2(t)$ and to integrate over a time equal to a bit-keying-element period T_B , centered about the time t_l the midpoint of the l th expected bit interval. The transmitted waveform is constructed as a linear superposition of $h_1(t)$ and $h_2(t)$ according to

$$h(t) = X_l h_1(t) + Y_l h_2(t). \quad (1)$$

The outputs of the integrators will yield the values of X_l and Y_l which contain the transmitted information,

$$X_l = (T_B)^{-1} \int_{t_l - T_B/2}^{t_l + T_B/2} h_1(t) h(t) dt \quad (2)$$

and

$$Y_l = (T_B)^{-1} \int_{t_l - T_B/2}^{t_l + T_B/2} h_2(t) h(t) dt, \quad (3)$$

as long as $h_1(t)$ and $h_2(t)$ are orthonormal to each other:

$$(T_B)^{-1} \int_{t_l - T_B/2}^{t_l + T_B/2} h_i(t) h_j(t) dt = \delta_{ij}. \quad (4)$$

Here δ_{ij} is the Kronecker delta function, equal to zero for $i \neq j$ and equal to 1 for $i = j$.

Correlation of Orthogonal Waveforms

A set of orthogonal wideband waveforms $h_1(t)$ and $h_2(t)$ can be generated by using a baseband waveform $h_B(t)$ to modulate both a sinusoidal and cosinusoidal wave:

$$h_1(t) = h_B(t) \cos \omega_0 t, \quad (5)$$

$$h_2(t) = h_B(t) \sin \omega_0 t, \quad (6)$$

$$h(t) = h_B(t)(X_l \cos \omega_0 t + Y_l \sin \omega_0 t). \quad (7)$$

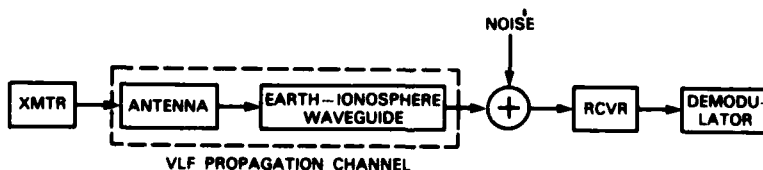


Fig. 4 — Model of the communication system

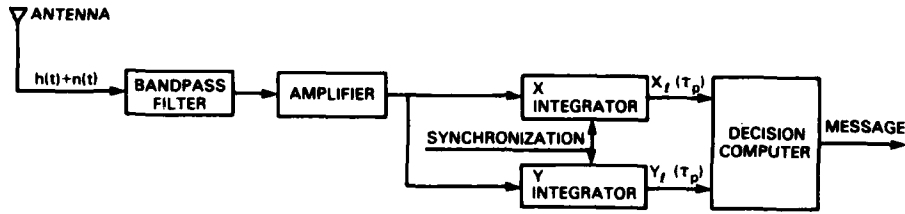


Fig. 5 — Model of the receiver-demodulator

The values of X_I and Y_I give the strength of the cosinusoidal and sinusoidal components. A correlation receiver can then be made to extract the value of X_I and Y_I :

$$X_I = 2(T_B)^{-1} \int_{t_i - T_B/2}^{t_i + T_B/2} h_B(t) (X_I \cos \omega_0 t + Y_I \sin \omega_0 t) h_B(t) \cos \omega_0 t dt \quad (8)$$

and

$$Y_I = 2(T_B)^{-1} \int_{t_i - T_B/2}^{t_i + T_B/2} h_B(t) (X_I \cos \omega_0 t + Y_I \sin \omega_0 t) h_B(t) \sin \omega_0 t dt. \quad (9)$$

A propagation delay time of τ_p modifies the correlator outputs to give new ones which we call $X_I(\tau_p)$ and $Y_I(\tau_p)$:

$$X_I(\tau_p) = 2(T_B)^{-1} \int_{t_i - T_B/2}^{t_i + T_B/2} h_B(t + \tau_p) [X_I \cos \omega_0(t + \tau_p) + Y_I \sin \omega_0(t + \tau_p)] \times h_B(t) \cos \omega_0 t dt \quad (10)$$

and

$$Y_I(\tau_p) = 2(T_B)^{-1} \int_{t_i - T_B/2}^{t_i + T_B/2} h_B(t + \tau_p) [X_I \cos \omega_0(t + \tau_p) + Y_I \sin \omega_0(t + \tau_p)] \times h_B(t) \sin \omega_0 t dt. \quad (11)$$

We find that the vector $\bar{R}_I(\tau_p) = (X_I(\tau_p), Y_I(\tau_p))$ is approximately the phase-rotated version of $\bar{R}_I = (X_I, Y_I)$. We have

$$X_I(\tau_p) = T_B^{-1} (X_I \cos \omega_0 \tau_p + Y_I \sin \omega_0 \tau_p) \int_{t_i - T_B/2}^{t_i + T_B/2} h_B(t) h_B(t + \tau_p) dt \quad (12)$$

and

$$Y_I(\tau_p) = T_B^{-1} (-X_I \sin \omega_0 \tau_p + Y_I \cos \omega_0 \tau_p) \int_{t_i - T_B/2}^{t_i + T_B/2} h_B(t) h_B(t + \tau_p) dt. \quad (13)$$

Thus we can write this equation in vector form if $\bar{R}_I = (X_I, Y_I)$:

$$\bar{R}_I(\tau_p) = T_B^{-1} \left[\int_{t_i - T_B/2}^{t_i + T_B/2} h_B(t) h_B(t + \tau_p) dt \right] \begin{bmatrix} \cos \omega_0 \tau_p & \sin \omega_0 \tau_p \\ -\sin \omega_0 \tau_p & \cos \omega_0 \tau_p \end{bmatrix} \bar{R}_I. \quad (14)$$

The magnitude of the vector $\bar{R}_I(\tau_p) = [X_I(\tau_p)^2 + Y_I(\tau_p)^2]^{1/2}$ is given by

$$|\bar{R}_I(\tau_p)| = T_B^{-1} |\bar{R}_I| \int_{t_i - T_B/2}^{t_i + T_B/2} h_B(t) h_B(t + \tau_p) dt. \quad (15)$$

The phase of the vector $\bar{R}_I(\tau_p)$ is given by

$$\phi_I(\tau_p) = \arg(X_I(\tau_p) + iY_I(\tau_p)) = \arg(X_I + iY_I) + \omega_0 \tau_p. \quad (16)$$

Thus, the magnitude of the $\bar{R}_I(\tau_p)$ vector varies slowly with τ_p , and the phase $\phi_I(\tau_p)$ changes rapidly.

Correlation of Other Orthogonal Waveforms

A more complicated set of orthogonal waveforms can be generated using two orthogonal baseband waveforms $h_{B1}(t)$ and $h_{B2}(t)$ such that for $i, j = 1, 2$

$$(T_B)^{-1} \int_{t-T_B/2}^{t+T_B/2} h_{B1}(t) h_{Bj}(t) dt = \delta_{ij}, \quad (17)$$

where δ_{ij} is the Kronecker delta function. The transmitted waveform $h(t)$ is given by

$$h(t) = X_i h_{B1}(t) \cos \omega_0 t + Y_i h_{B2}(t) \sin \omega_0 t. \quad (18)$$

To extract the value of X_i and Y_i from this waveform, we need a correlator receiver to do the following integrations:

$$X_i = 2(T_B)^{-1} \int_{t-T_B/2}^{t+T_B/2} [X_i h_{B1}(t) \cos \omega_0 t + Y_i h_{B2}(t) \sin \omega_0 t] [h_{B1}(t) + h_{B2}(t)] \cos \omega_0 t dt \quad (19)$$

and

$$Y_i = 2(T_B)^{-1} \int_{t-T_B/2}^{t+T_B/2} [X_i h_{B1}(t) \cos \omega_0 t + Y_i h_{B2}(t) \sin \omega_0 t] [h_{B1}(t) + h_{B2}(t)] \sin \omega_0 t dt. \quad (20)$$

When the time of arrival is changed to $t = t + \tau_p$, we have

$$\begin{aligned} X_i(\tau_p) &= 2(T_B)^{-1} \int_{t-T_B/2}^{t+T_B/2} [X_i h_{B1}(t + \tau_p) \cos \omega_0(t + \tau_p) + Y_i h_{B2}(t + \tau_p) \sin \omega_0(t + \tau_p)] \\ &\quad \times [h_{B1}(t) + h_{B2}(t)] \cos \omega_0 t dt \end{aligned} \quad (21)$$

and

$$\begin{aligned} Y_i(\tau_p) &= 2(T_B)^{-1} \int_{t-T_B/2}^{t+T_B/2} [X_i h_{B1}(t + \tau_p) \cos \omega_0(t + \tau_p) + Y_i h_{B2}(t + \tau_p) \sin \omega_0(t + \tau_p)] \\ &\quad \times [h_{B1}(t) + h_{B2}(t)] \sin \omega_0 t dt. \end{aligned} \quad (22)$$

This gives

$$\begin{aligned} X_i(\tau_p) &= X_i \cos \omega_0 \tau_p T_B^{-1} \int h_{B1}(t + \tau_p) [h_{B1}(t) + h_{B2}(t)] dt \\ &\quad + Y_i \sin \omega_0 \tau_p T_B^{-1} \int h_{B2}(t + \tau_p) [h_{B1}(t) + h_{B2}(t)] dt \end{aligned} \quad (23)$$

and

$$\begin{aligned} Y_i(\tau_p) &= -X_i \sin \omega_0 \tau_p T_B^{-1} \int_{t-T_B/2}^{t+T_B/2} h_{B1}(t + \tau_p) [h_{B1}(t) + h_{B2}(t)] dt \\ &\quad + Y_i \cos \omega_0 \tau_p T_B^{-1} \int_{t-T_B/2}^{t+T_B/2} h_{B2}(t + \tau_p) [h_{B1}(t) + h_{B2}(t)] dt. \end{aligned} \quad (24)$$

If the two baseband modulation functions are sufficiently orthogonal that

$$T_B^{-1} \int_{t-T_B/2}^{t+T_B/2} h_{B1}(t + \tau_p) h_{B2}(t) dt \approx 0 \quad (25)$$

and sufficiently similar that

$$T_B^{-1} \int_{t-T_B/2}^{t+T_B/2} h_{B1}(t + \tau_p) h_{B1}(t) dt = T_B^{-1} \int_{t-T_B/2}^{t+T_B/2} h_{B2}(t + \tau_p) h_{B2}(t) dt, \quad (26)$$

we again obtain

$$X_i(\tau_p) = (X_i \cos \omega_0 \tau_p + Y_i \sin \omega_0 \tau_p) T_B^{-1} \int_{t-T_B/2}^{t+T_B/2} h_{B1}(t + \tau_p) h_{B1}(t) dt \quad (27)$$

and

$$Y_i(\tau_p) = (-X_i \sin \omega_0 \tau_p + Y_i \cos \omega_0 \tau_p) T_B^{-1} \int_{t-T_B/2}^{t+T_B/2} h_{B1}(t+\tau_p) h_{B1}(t) dt. \quad (28)$$

When the more complicated correlators of Eqs. (19) and (20) are used, and the orthogonal waveforms satisfy the conditions of Eqs. (25) and (26), the type of waveform of Eq. (18) gives a behavior similar to that of Eq. (7).

Modulation Methods

The values of \bar{R}_i can be modified at the transmitter to initiate the communication of information. In amplitude modulation the magnitude of \bar{R}_i is varied. In phase-shift keying the phase angle ϕ_i is modulated. Thus, in general, information may be transmitted by changing the transmitted vector \bar{R}_i in some prescribed way. The stability of the received vector $\bar{R}_i(\tau_p)$ in amplitude and phase is important in the performance of communication systems. In the realistic communication channel the values of $\bar{R}_i(\tau_p)$ will also depend on the noise present. In this study we neglect noise and simply study the effects of propagation on $\bar{R}_i(\tau_p)$.

MSK Signals

In the field of VLF communications, minimum shift keying (MSK) is a commonly used type of spread-spectrum modulation. MSK is mathematically described in terms of a transmitted waveform $s(t)$, a baseband modulation $u(t)$, and a chip waveform $p(t)$, as follows:

$$s(t) = \text{Re} \left[u(t) e^{i\omega_0 t} \right], \quad (29)$$

$$u(t) = \sum_{n=0}^{\frac{N}{2}-1} \left[X_i I_n p(t - nT) - i Y_i Q_n p(t - T/2 - nT) \right], \quad (30)$$

$$p(t) = \begin{cases} \sqrt{\frac{2}{T}} \left[\cos \left(\frac{\pi t}{T} \right) \right], & -T/2 \leq t \leq T/2, \\ 0, & |t| > T/2. \end{cases} \quad (31)$$

This is a specific version of the signal described in general by Eq. (18), in which the orthogonal baseband waveforms $h_{B1}(t)$ and $h_{B2}(t)$ are given by

$$h_{B1}(t) = \sqrt{T} \sum_{n=0}^{\frac{N}{2}-1} I_n p(t - nT) \quad (32)$$

and

$$h_{B2}(t) = \sqrt{T} \sum_{n=0}^{\frac{N}{2}-1} Q_n p(t - T/2 - nT). \quad (33)$$

In these above equations I_n and Q_n are pseudorandomly chosen integers of value +1 or -1. It is assumed that both the transmitter and receiver possess synchronized pseudorandom-number-sequence generators that provide the I_n and Q_n sequences. The frequency ω_0 is the carrier frequency of the broadcast. The time interval T is the duration of a chip. Since two chips are transmitted during each chip duration, the chip length τ_c is $T/2$. The MSK modulation method gives rise to a constant-amplitude waveform with continuous phase as long as X_i and Y_i are equal to ± 1 . The bandwidth of the transmitted signal is inversely related to the chip period. The value of the waveform $s(t)$ depends on one value of I_n and one value of Q_n simultaneously except at the instant when a transition is being

made from one value of I_n or Q_n to the next. At the transition time the amplitude of the waveform undergoing transition is zero, because the $p(t)$ function goes smoothly to zero at the beginning and end of its range. At that instant the value of $s(t)$ depends only on the other integer Q_n or I_n . Let us consider the autocorrelation function $B(\tau)$ for the MSK waveform $s(t)$:

$$B(\tau) = \lim_{T' \rightarrow \infty} \frac{1}{T'} \int_0^{T'} s(t)s(t+\tau) dt. \quad (34)$$

Use of $s(t)$ from Eq. (29) will make $B(\tau)$ nonzero as long as $|\tau| < T$. When $|\tau| > T$, the contributions to $B(\tau)$ will all be from terms having the products $Q_n I_m$, $Q_n Q_m$, and $I_n I_m$ with $n \neq m$. These terms are as often +1 as they are -1 for an orthogonal or uncorrelated set of $\{Q_n\}$ and $\{I_n\}$; so a summation based on these values should remain small. Thus a large value for the autocorrelation function occurs only for $|\tau| < T$, when I_n^2 and Q_n^2 terms contribute. Since $I_n^2 = Q_n^2 = 1$, these terms are easy to evaluate. The correlation vector $\bar{R}_l(\tau_p)$ is closely related to the autocorrelation function $B(\tau)$. At very low frequencies the electromagnetic waves may be considered to propagate by distinct waveguide modes or hops. The time delays between dominant modes and hops are small—less than a millisecond [6]—producing the coherent overlap of one chip with its time-delayed image. At some receiver locations the interference of the two waves with each other results in "selective" fading. Such fading is called "selective" because it occurs only for frequencies for which the interference condition is satisfied. At other nearby receiver locations or frequencies the time delays will be such as to produce two pulses which reenforce each other. The propagation channel can be simulated by a multipath model in which $h_T(t)$ is the transmitted wave and the received wave is

$$h_R(t) = \sum_{i=1}^N A_i h_T(t - \tau_i), \quad (35)$$

where τ_i is the propagation time for the i th mode or hop and A_i is the amplitude for the i th mode or hop. In the case of earth-ionosphere waveguide propagation sometimes the waves have distinctly different group and phase velocities. Then, we must consider both the phase and group delay times $\tau_p^{(i)}$ and $\tau_g^{(i)}$. The phase delay of the baseband modulation is governed by $\tau_p^{(i)}$, and the group delay is governed by $\tau_g^{(i)}$.

THE MSK CORRELATION RECEIVER

One can readily evaluate the performance of a correlation receiver for MSK modulation and coherent detection for signal reception on a *single-path* propagation channel. The correlation vector $\bar{R}_l(\tau_p)$ obtained when one uses MSK modulation is explicitly calculated by substituting the expression for $h_{B1}(t)$ from Eq. (32) into Eqs. (27) and (28). The integral $I_B(\tau_p)$, defined as

$$\begin{aligned} I_B(\tau_p) &= T_B^{-1} \int_{t-T_B/2}^{t+T_B/2} h_{B1}(t+\tau_p) h_{B1}(t) dt \\ &= T_B^{-1} \sum_{n=0}^{N/2-1} I_n I_{n'} \int_{t-T_B/2}^{t+T_B/2} p(t-nT) p(t+\tau_p-nT) dt, \end{aligned} \quad (36)$$

is readily evaluated. The limits of integration in this equation extend far beyond the region of variable t , for which the integrand is nonzero. We can change the integration variable to

$$t' = t - nT. \quad (37)$$

The limits of integration are thereby changed to $t_1 + T_B/2 - nT$ and $t_1 - T_B/2 - nT$:

$$I_B(\tau_p) = T_B^{-1} \sum_{n=0}^{N/2-1} I_n I_{n'} \int_{t_1-T_B/2-nT}^{t_1+T_B/2-nT} p(t') p(t' + \tau_p - nT) dt'. \quad (38)$$

Since $p(t') = 0$, for $|t'| > T/2$, we need integrate only between $-T/2 \leq t' \leq T/2$. We obtain

$$I_B(\tau_p) = T_B^{-1} \sum_{\substack{n=0 \\ n'=0}}^{\frac{N}{2}-1} I_n I_{n'} \int_{-T/2}^{+T/2} p(t') p(t' + \tau_p + (n - n')T) dt. \quad (39)$$

From this formulation we see that the integral depends only on the difference between n and n' and not on the individual values of n and n' separately. Let us define

$$C_k(\tau_p) = \int_{-T/2}^{+T/2} p(t') p(t' + \tau_p + kT) dt. \quad (40)$$

Since $k = n - n'$, Eq. (39) becomes

$$\begin{aligned} I_B(\tau_p) &= T_B^{-1} \sum_{\substack{n=0 \\ n'=0}}^{\frac{N}{2}-1} I_n I_{n'} C_{n-n'}(\tau_p) \\ &= T_B^{-1} \sum_{n=0}^{\frac{N}{2}-1} \sum_{k=n}^{\frac{N}{2}-1} I_n I_{n-k} C_k(\tau_p) \\ &= T_B^{-1} \sum_{n=0}^{\frac{N}{2}-1} \sum_{k=-\left[\frac{N}{2}-1\right]}^{\frac{N}{2}-1} I_n I_{n-k} C_k(\tau_p) U_{n-k}, \end{aligned} \quad (41)$$

where

$$\begin{aligned} U_{n-k} &= 1, & \text{if } 0 \leq n-k \leq \frac{N}{2}-1, \\ &= 0, & \text{if } n-k < 0 \text{ or } n-k > \frac{N}{2}-1. \end{aligned}$$

We then interchange the order of summation in Eq. (41) to get

$$I_B(\tau_p) = T_B^{-1} \sum_{k=-\left[\frac{N}{2}-1\right]}^{\frac{N}{2}-1} C_k(\tau_p) \sum_{n=0}^{\frac{N}{2}-1} I_n I_{n-k} U_{n-k}. \quad (42)$$

Because of the orthogonality of the set $\{I_n\}$ with any sequentially shifted copy of itself, we can write

$$\sum_{n=0}^{\frac{N}{2}-1} I_n I_{n-k} U_{n-k} = \frac{N}{2} \delta_{k,0}. \quad (43)$$

This assumes that the binary sequence $\{I_n\}$ has been generated by a method which has "good" autocorrelation properties for the pseudo-noise-coding application [7]. We obtain

$$I_B(\tau_p) = \frac{NT_B^{-1}}{2} C_0(\tau_p). \quad (44)$$

To calculate $C_0(\tau_p)$, we substitute into Eq. (40)

$$C_0(\tau_p) = \int_{-T/2}^{+T/2} p(t') p(t' + \tau_p) dt. \quad (45)$$

The value of $C_0(\tau_p)$ is symmetric with respect to τ_p and can be obtained by using elementary integration methods:

$$\begin{aligned}
C_0(\tau_p) &= \frac{4}{T} \int_{-\frac{T}{2}}^{T/2-\tau_p} p(t') p(t' + \tau_p) dt, \quad \text{if } \tau_p \geq 0, \\
&= \frac{4}{T} \int_{-\frac{T}{2}}^{T/2-\tau_p} \cos \left[\frac{\pi t'}{T} \right] \cos \left[\pi \left(\frac{t' + \tau_p}{T} \right) \right] dt' \\
&= \frac{4}{T} \left[\left(1 - \frac{|\tau_p|}{T} \right) \cos \frac{\pi \tau_p}{T} + \frac{1}{\pi} \sin \frac{|\tau_p|}{T} \right]
\end{aligned} \tag{46}$$

Equations (27) and (28) become

$$X_i(\tau_p) = (X_i \cos \omega_0 \tau_p + Y_i \sin \omega_0 \tau_p) NT_B^{-1} C_0(\tau_p) \tag{47a}$$

and

$$Y_i(\tau_p) = (-X_i \sin \omega_0 \tau_p + Y_i \cos \omega_0 \tau_p) NT_B^{-1} C_0(\tau_p). \tag{47b}$$

In matrix form we have

$$\bar{R}_i(\tau_p) = NT_B^{-1} T^{-1} \begin{pmatrix} \cos \omega_0 \tau_p & \sin \omega_0 \tau_p \\ -\sin \omega_0 \tau_p & \cos \omega_0 \tau_p \end{pmatrix} \bar{R}_i C_0(\tau_p). \tag{47c}$$

A receiver can be adaptively synchronized to the incoming signal by introducing a variable delay τ_R into the stream of baseband keying elements to generate a family of ideal baseband keying elements h_{B1} and h_{B2} . Mathematically this simply means the introduction of the variable $t + \tau_R$ into the expression for h_{B1} in Eqs. (27) and (28) in place of t . The selection of the synchronization time τ_R can greatly affect receiver performance when the actual propagation delay time τ_p is unknown (or equivalently the clocks that generate the chip streams are not in perfect initial synchronism). Therefore we rewrite Eq. (47c) to exhibit the dependence of system performance on τ_R . We obtain the following expression for $\bar{R}_i(\tau_p, \tau_R)$:

$$\bar{R}_i(\tau_p, \tau_R) = NT_B^{-1} \begin{pmatrix} \cos \omega_0 \tau_p & \sin \omega_0 \tau_p \\ -\sin \omega_0 \tau_p & \cos \omega_0 \tau_p \end{pmatrix} \bar{R}_i C_0(\tau_p - \tau_R). \tag{48}$$

The magnitude of the components of $\bar{R}_i(\tau_p, \tau_R)$ are proportional to the in-phase and quadrature components of the received radio-frequency carrier wave because of the multipliers $\cos \omega_0 \tau_p$ and $\sin \omega_0 \tau_p$ in the matrix. However, the magnitude of $\bar{R}_i(\tau_p, \tau_R)$ depends on the propagation delay time τ_p and on the receiver time τ_R by the factor $\tau_p - \tau_R$. If the receiver is badly out of synchronization, this factor can be zero or very small. If the receiver is employing phase-shift keying, any change in the propagation time τ_p , even after the receiver is perfectly synchronized on the chip ($0 \approx |\tau_p - \tau_R| \ll T$), will induce a corresponding phase change in the phase of the vector $\bar{R}_i = (\tau_p, \tau_R)$; that is, the doppler phase variation of the radio-frequency carrier induces an equal doppler shift on the phase angle ϕ_R . These types of doppler-signal phase variations are often seen when an mobile transmitter or receiver is used. In such a circumstance we cannot assume $\tau_p(t)$ will be constant at each instant within a bit period to permit the factorization shown in Eqs. (21) and (22). However, the other manipulations that we performed on the expression for \bar{R} are all valid up to this point. To obtain the resultant correlation vector $\bar{R}_i(\tau_p, \tau_R)$ if the delay time is slowly changing within a bit period, we must average the instantaneous values of $\bar{R}_i[\tau_p(t), \tau_p]$ over an entire bit period:

$$\bar{R}_i(\tau_p, \tau_R) = NT_B^{-1} T^{-1} \int_{t-T/2}^{t+T/2} \begin{pmatrix} \cos \omega_0 \tau_p(t) & \sin \omega_0 \tau_p(t) \\ -\sin \omega_0 \tau_p(t) & \cos \omega_0 \tau_p(t) \end{pmatrix} \bar{R}_i C_0[\tau_p(t) - \tau_R] dt. \tag{49}$$

From this expression one can approximately evaluate the affect on the $\bar{R}_i = [\tau_p(t), \tau_R]$ vector for various conditions of $\tau_p(t)$ and synchronization conditions for a single path propagation.

We have reviewed the elementary cases of a stationary and moving transmitter having a single path of propagation, because this is the simplest case. Linear superposition holds for the waves and correlation procedures; so a resultant from a case having several propagation paths can be obtained by addition of terms from single-path cases.

TWO PROPAGATION MODES AND A STATIONARY TRANSMITTER

When a stationary transmitter produces a signal at a receiver that comes by two propagation paths, there are two propagation delay times τ_{p1} and τ_{p2} and two (real-valued) amplitudes of the two modes A_1 and A_2 . Alternatively, we may say that each mode is described by a complex amplitude, with the magnitude of each complex amplitude being the real amplitude and the phase being related to the propagation time. The voltage impressed on the receiving antenna by the received signal represents a waveform that is the sum of two time-delayed replicas of the initial waveform. Let the subscript i denote the mode index. Then we will get the following expression for the total correlation vector $\bar{R}^T(\tau_R)$:

$$\begin{aligned}\bar{R}_i^T(\tau_R) &= \sum_{i=1}^2 \bar{R}_i(\tau_{p,i}, \tau_R) \\ &= NT_b^{-1} T^{-1} \sum_{i=1}^2 A_i \begin{bmatrix} \cos \omega_0 \tau_{p,i} & \sin \omega_0 \tau_{p,i} \\ -\sin \omega_0 \tau_{p,i} & \cos \omega_0 \tau_{p,i} \end{bmatrix} \begin{bmatrix} X_i \\ Y_i \end{bmatrix} C_0(\tau_{p,i} - \tau_R).\end{aligned}\quad (50)$$

The behavior of $\bar{R}_i^T(\tau_R)$ as a function of the receiver chip synchronization time τ_R can be quite different from the behavior when there is only a single path. A splitting of the correlation peak can occur. Indeed, instead of the correlation being best when $\tau_{p,i} = \tau_R$, it could be bad at this time. Numerical examples given later exhibit this circumstance.

FIELD-STRENGTH EXPRESSIONS

For the case of an antenna trailing behind an airborne transmitting facility, the correlation vectors generated by both the horizontal and vertical components of the antenna are included in $\bar{R}_i^T(\tau_R)$. For an inclined short dipole antenna, the endfire-generated components are modified by $\cos \zeta \sin \gamma$, and the broadside generation depends on $\sin \zeta \sin \gamma$, where ζ is the angle between the horizontal portion of the inclined dipole and the great circle path to the receiver and γ is the inclination angle of the antenna measured from the vertical. The expression for the resultant vertical electric field $E_r(D)$ at distance D from the transmitter can be written as follows [4, p. 332]:

$$E_r(D) = \cos \gamma E_r^{ve} + \sin \gamma E_r^{he}. \quad (51)$$

In this expression

$$E_r^{ve} = \frac{-\eta I ds}{h \sqrt{a \lambda \sin \theta}} \sum_q S_q^{1.5} \Lambda_q^e G_q^e(z_s) G_q^e(z) \exp(ik_0 D S_q - i\pi/4) \quad (52)$$

and

$$\begin{aligned}E_r^{he} &= \frac{-\eta I ds}{h \sqrt{a \lambda \sin \theta}} \sum_q \left[\Lambda_q^e G_q^e(z_s) \Delta_q^e(z_s) \cos \zeta \right. \\ &\quad \left. + \frac{\eta \Lambda_q^h G_q^h(z_s)}{Z_{eh}} \sin \zeta \right] S_q^{1/2} G_q^e(z) \exp(ik_0 D S_q - i\pi/4).\end{aligned}\quad (53)$$

The quantities in these expressions are explained in Ref. 4 and are summarized below:

Λ_q^v	is the excitation factor of the q th mode for a vertically polarized electric dipole,
Λ_q^h	is the excitation factor of the q th mode for a horizontally polarized electric dipole,
$G_q^v(z)$	is the height-gain function of the quasi-TM vertical electric-field component,
$G_q^h(z)$	is the height-gain function of the quasi-TE vertical magnetic-field component
S_q	is the sine of the complex eigenangle of the q th waveguide mode,
z	is the height of the receiver,
z_t	is the height of the transmitter,
a	is the radius of the earth,
$D = a\theta$	is the great-circle distance between the transmitter and the receiver,
$\Delta_q^v(z)$	is the normalized impedance of the quasi-TM-mode fields,
$\Delta_q^h(z)$	is the normalized impedance of the quasi-TE-mode fields,
Z_{eh}	is the coupling impedance in the mode $= E_\phi(0)/H_\phi(0)$ at the earth's surface,
η	is the impedance of free space;
k_0	is the free-space propagation constant $(= \omega/c)$ for an electromagnetic wave of frequency ω_0 ,
h	is the reference height of the ionosphere,
λ	is the space wavelength, and
$I ds$	is the current moment.

The dispersion that occurs on each individual waveguide mode is usually minimal when well-behaved types of D- and E-region boundary conditions are present [6]. Each individual waveguide mode can be considered as a dispersionless path over a sufficiently narrow fractional bandwidth. The effect of propagation is to produce several time-delayed images of the transmitted waveform at the receiver. The amplitudes of these waveform images vary independently with time, as the inclined antenna is transported about by the aircraft. This variation with position of the aircraft can be modeled readily by letting the amplitudes $\{A_i\}$ and delay times $\{\tau_{p,i}\}$ vary in an appropriate way.

CORRELATION EFFECTS OF ANTENNA ROTATION

It is easy to show the effects of rotation by an inclined elevated antenna given the previous development of the mathematics. The horizontal component of the inclined antenna generates both TE and TM modes according to Eq. (53), because the horizontally generated fields have phases and amplitudes different from those generated by the vertical antenna components. The waveguide modal interference pattern for an elevated horizontal antenna differs from that of a vertical antenna. This effect is illustrated in Fig. 6 (taken from Ref. 3), which shows the fields generated by variously inclined antennas at 20 kHz. The amplitudes of the horizontally generated fields vary as the cosine of the angle between the horizontal antenna component and the direction of propagation.

In simulating the effect of this variation on the receiver output vector, we use Eq. (50) for the received correlation vectors, and we use four amplitudes $\{A_i\}$, four phase time delays $\{\tau_p\}$, and four group time delays $\{\tau_g\}$. Two of the amplitudes represent two vertically generated mode fields and vary as $\sin \gamma$. The other two represent horizontally generated TM mode fields and vary as the product $\cos \zeta \cos \gamma$. The resultant expression for the correlator output is the same as Eq. (50) except that in this case the correlation output is the summation of the outputs for the four individual modes.

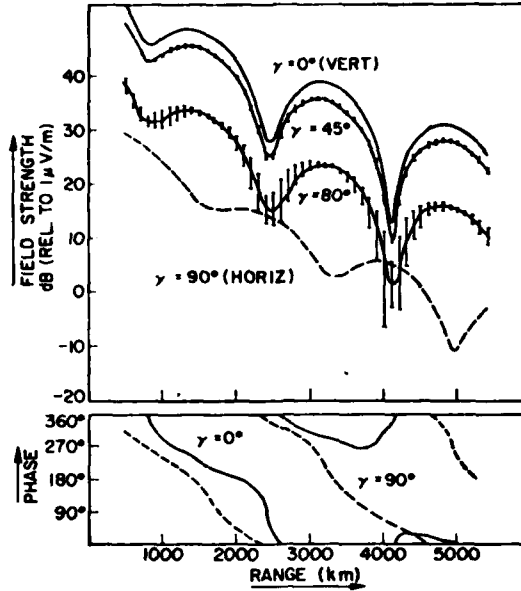


Fig 6 — Predicted variation of field strength and phase with distance for 20 kHz and vertical, inclined, and horizontal antenna inclinations

Denoting the $X_i^{(i)}(\tau_R)$ from the vertically electrically generated modes as $X_i^{(i)ve}(\tau_R)$ and the $X_i^{(i)}(\tau_R)$ from the horizontally electrically generated modes as $X_i^{(i)he}(\tau_R)$, we can write

$$X_i^T(\tau_R) = \cos \gamma \sum_{i=1}^{N'} X_i^{(i)ve}(\tau_R) + \cos \zeta \sin \gamma \sum_{i=1}^{N'} X_i^{(i)he}(\tau_R). \quad (54)$$

Parallel definitions can be made for $Y_i^T(\tau_R)$, $Y_i^{(i)ve}(\tau_R)$ and $Y_i^{(i)he}(\tau_R)$, and we obtain

$$Y_i^T(\tau_R) = \cos \gamma \sum_{i=1}^{N'} Y_i^{(i)ve}(\tau_R) + \cos \zeta \sin \gamma \sum_{i=1}^{N'} Y_i^{(i)he}(\tau_R). \quad (55)$$

The vector $\bar{R}_i^T(\tau_R)$ is a sum of two vectors $\bar{R}_i^{he}(\tau_R)$ and $\bar{R}_i^{ve}(\tau_R)$:

$$\bar{R}_i^T(\tau_R) = \cos \gamma \bar{R}_i^{ve}(\tau_R) + \cos \zeta \sin \gamma \bar{R}_i^{he}(\tau_R). \quad (56)$$

The vectors $\bar{R}_i^{ve}(\tau_R)$ and $\bar{R}_i^{he}(\tau_R)$ can be parallel, perpendicular, or opposed to each other, depending on circumstances and the value of τ_R . The resultant $\bar{R}_i^T(\tau_R)$ vector can change quite dramatically during a complete orbit. For example, if $\bar{R}_i^{ve}(\tau_R)$ and $\bar{R}_i^{he}(\tau_R)$ are of the same magnitude and phase, there would be one large oscillation of $|\bar{R}_i^T(\tau_R)|$ per orbit (provided $\gamma = 45^\circ$). If $\bar{R}_i^{ve}(\tau_R)$ and $\bar{R}_i^{he}(\tau_R)$ are perpendicular to each other, there would be two oscillations of $|\bar{R}_i^T(\tau_R)|$ with one cycle ζ . There is a mathematical isomorphism between the phasor $E_r(D)$ and the vector $\bar{R}_i^T(\tau_R)$, since the composition of various phasors which form the complex phasor sum $E_r(D)$ is isomorphic to the composition of various correlation vectors which form the two-dimensional correlation vector sum $\bar{R}_i^T(\tau_R)$. When both TE and TM waveguide mode propagation from an airborne transmitting facility are taken into account, we obtain

$$\bar{R}_i^T(\tau_R) = \bar{R}_i^{ve}(\tau_R) \cos \gamma + \sin \gamma [\cos \zeta \bar{R}_i^{he}(TM, \tau_R) + \sin \zeta \bar{R}_i^{he}(TE, \tau_R)]. \quad (57)$$

The total vector $\bar{R}_I^T(\tau_R)$ is the sum of independently propagated vertical endfire- and broadside-generated components. These components are themselves sums of components which are propagated by different waveguide modes.

DIAGRAMMATIC REPRESENTATIONS

It is instructive to view diagrams that illustrate the behavior of the various \bar{R}_I vectors as τ_R and ζ vary. The following example illustrates what can happen in a particularly severe case of modal interference. Figure 7 depicts the variation of a single-mode correlation output $\bar{R}_I^{(1)ve}(\tau_R)$ from a stationary vertical electric transmitter. Figure 8 shows an output function $\bar{R}_I^{(2)ve}(\tau_R)$ for a signal coming slightly later on a second-order mode and 180° out of phase with the first. Figure 9 gives the resultant $\bar{R}_I^{ve}(\tau_R)$, which is the sum of the correlation outputs of the first and second modes. Figure 10 shows the phase of the vector $\bar{R}_I^{ve}(\tau_R)$ as a function of τ_R .

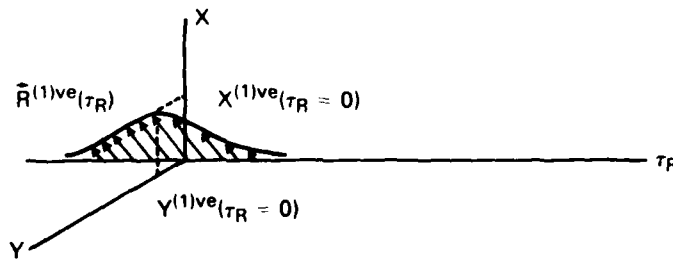


Fig. 7 — Graph of $\bar{R}_I^{(1)ve}(\tau_R)$ versus τ_R for a stationary vertical electric-dipole transmitter

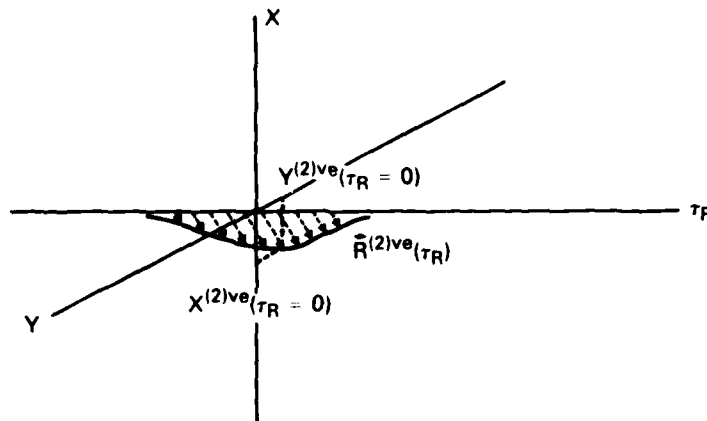


Fig. 8 — Graph of $\bar{R}_I^{(2)ve}(\tau_R)$ versus τ_R for a stationary vertical electric dipole transmitter. The phase of this wave is 180° opposite to that illustrated in Fig. 7. The maximum value of $|\bar{R}_I^{(2)ve}(\tau_R)|$ occurs at slightly greater τ_R values than does the maximum value of $|\bar{R}_I^{(1)ve}(\tau_R)|$ shown in Fig. 7.

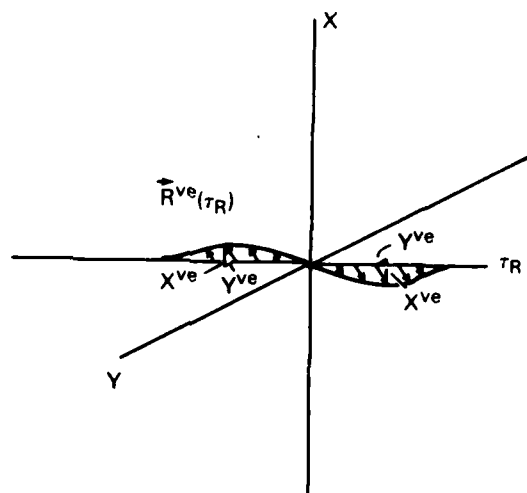


Fig. 9 — Graph of $\bar{R}_l^{ve}(\tau_R) = \bar{R}_l^{(1)ve}(\tau_R) + \bar{R}_l^{(2)ve}(\tau_R)$, showing an abrupt change of phase at $\tau_R = 0$ and a large shift in the value of τ_R for which $|\bar{R}_l^{ve}(\tau_R)|$ is greatest

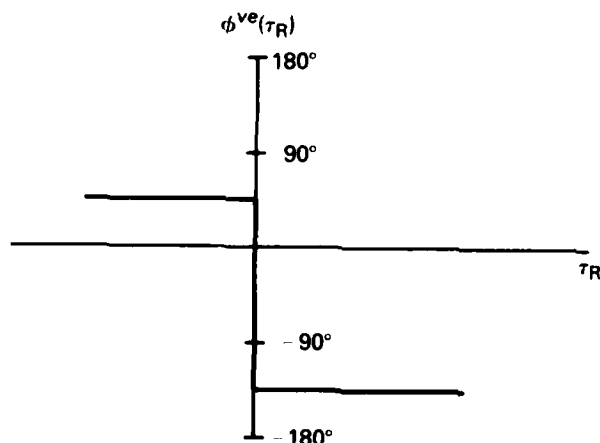


Fig. 10 — Graph of $\phi_l^{ve}(\tau_R)$, the angle of the $\bar{R}_l^{ve}(\tau_R)$ vector with the x axis in Fig. 9, showing an abrupt shift of phase at $\tau_R = 0$

Figure 11 shows the resultant $\bar{R}_I^T(\tau_R) = \cos \gamma \bar{R}_I^{ve}(\tau_R) + \sin \gamma \cos \zeta \bar{R}_I^{he}(\tau_R)$, where ζ is the angle between the direction of propagation and the endfire direction of the antenna. The angle γ is the inclination angle of the antenna; we take $\gamma = 45^\circ$ and $\zeta = 0$ for this example. Figure 12 shows the same resultant except for the condition $\zeta = 180^\circ$. The conditions for $\zeta = 90^\circ$ and $\zeta = 270^\circ$ are both shown by the pattern of Fig. 9, since $\bar{R}_I^T(\tau_R)$ is composed solely of the vertically generated modes in these cases. These figures give a picture of $\bar{R}_I^T(\tau_R)$ at the four cardinal points of an orbit.

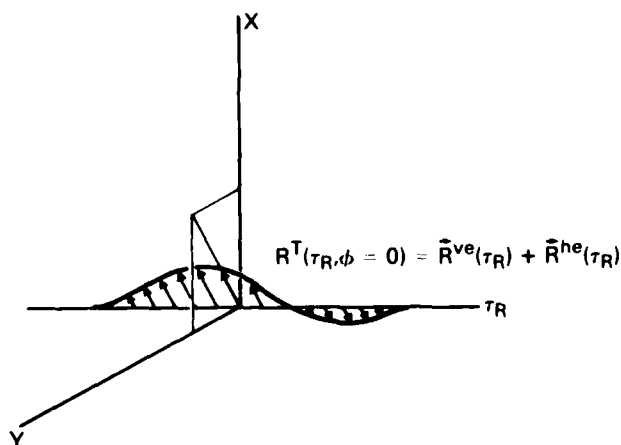


Fig. 11 - Graph of $\bar{R}_I^T(\tau_R)$ for an endfire case ($\cos \zeta = +1$), illustrating the change in the value of τ_R for which $|\bar{R}_I^T(\tau_R)| = 0$ and the variation in the size of the peak values of $|\bar{R}_I^T(\tau_R)|$ on opposite sides of $\tau_R = 0$. Here a relatively small value of $|\bar{R}_I^{he}(\tau_R)|$ is assumed.

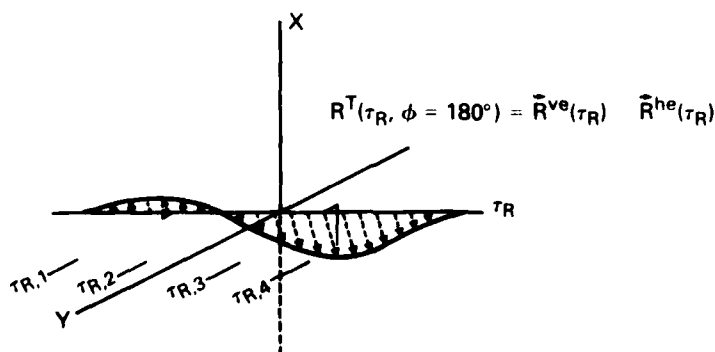


Fig. 12 - Graph of $\bar{R}_I^T(\tau_R)$ for the opposite endfire case ($\cos \zeta = -1$) to the case in Fig. 11. Here the largest value of $|\bar{R}_I^T(\tau_R)|$ occurs for $\tau_R > 0$ whereas, in Fig. 11 it was for $\tau_R < 0$. Synchronization times (τ_R) to be considered in subsequent figures are shown.

In Fig. 12 four sample synchronization times, designated τ_{R1} , τ_{R2} , τ_{R3} , and τ_{R4} , represent possible correlation times that might occur within a receiver. We look at the variation of the correlation vector magnitude $|\bar{R}_I^T(\tau_{Ri})|$ and phase $\phi_I^T(\tau_{Ri})$ during a complete orbit for these times. Figures 13 and 14 show the phase and magnitude of $\bar{R}_I^T(\tau_{R1})$. The phase is constant in this case, because $\bar{R}_I^{ve}(\tau_{R1})$ is greater than and parallel to $\bar{R}_I^{hw}(\tau_{R1})$. The magnitude varies in a mild way. In Figs. 15 and 16 showing the phase and amplitude for the time τ_{R2} , the phase makes two quick successive 180° changes in the neighborhood of $\zeta = 180^\circ$, and the amplitude goes through two successive nulls. Figures 17 and 18 give $\bar{R}_I^T(0)$. This vector varies cosinusoidally, because there is no contribution from the vertical electric antenna component. Figures 19 and 20 show the behavior of $\bar{R}_I^T(\tau_{R3})$, which is similar to the behavior of $\bar{R}_I^T(\tau_{R2})$ except that the nulls occur near $\zeta = 0^\circ$ rather than $\zeta = 180^\circ$. Figures 21 and 22 show the behavior of $\bar{R}_I^T(\tau_{R4})$, which is similar to $\bar{R}_I^T(\tau_{R1})$ except for a shift in orbit angle ζ of 180° .

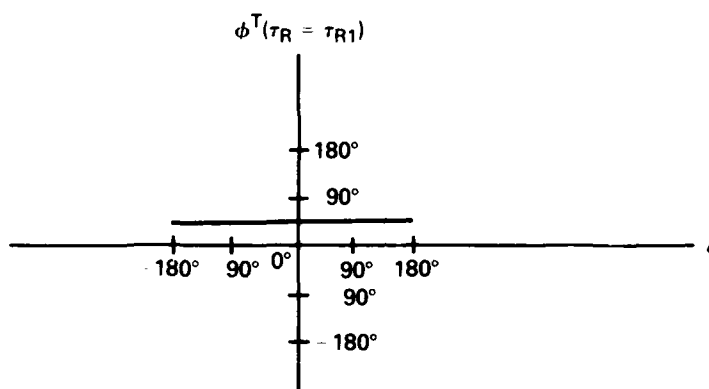


Fig. 13 — Graph of $\phi_I^T(\tau_{R1})$ as the angle of turn ζ of an inclined antenna changes from -180° to $+180^\circ$ for the synchronization time τ_{R1} . This phase is constant because the contribution of the vertical antenna component always exceeds that of the horizontal component for this synchronization time.

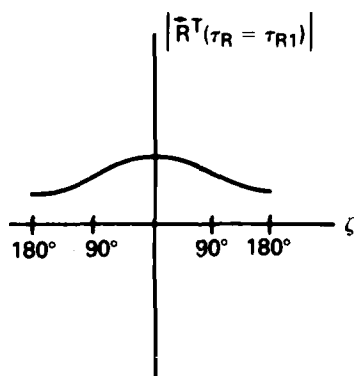


Fig. 14 — Graph of $|\bar{R}_I^T(\tau_{R1})|$ as ζ varies from -180° to $+180^\circ$. The relatively gentle variation of $|\bar{R}_I^T(\tau_{R1})|$ occurs because $|\bar{R}_I^{ve}(\tau_{R1})| > |\bar{R}_I^{hw}(\tau_{R1})|$.

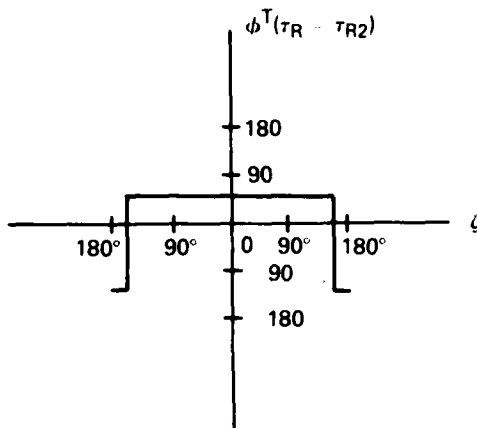


Fig. 15 — Graph of $\phi^T(\tau_{R2})$ versus orbit angle ζ . For this lock-on time there are two rapid and large phase changes near $\zeta = 180^\circ$

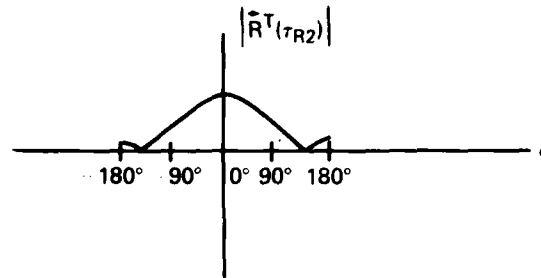


Fig. 16 — Graph of $|\tilde{R}^T(\tau_{R2})|$ versus orbit angle ζ , showing how this function goes to zero when $\phi^T(\tau_{R2})$ is making the abrupt phase transition

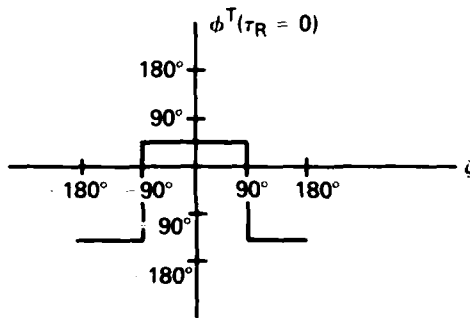


Fig. 17 — Graph of $\phi^T(\tau_R = 0)$ versus angle ζ . There is essentially no contribution from the vertical component for this value of τ_R , so the phase is controlled by the horizontal component of the transmitting antenna.

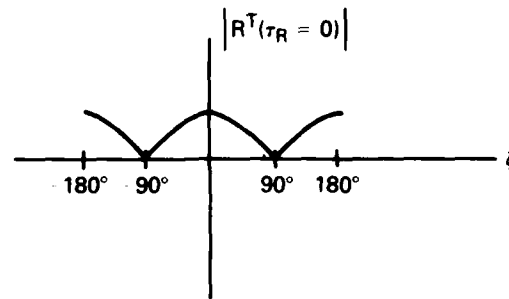


Fig. 18 — Graph of $|\tilde{R}^T(\tau_R = 0)|$ versus orbit angle ζ . The cosinusoidal variation is caused by the $\cos \zeta$ modulation of the horizontal component. The vertical component contributes essentially zero.

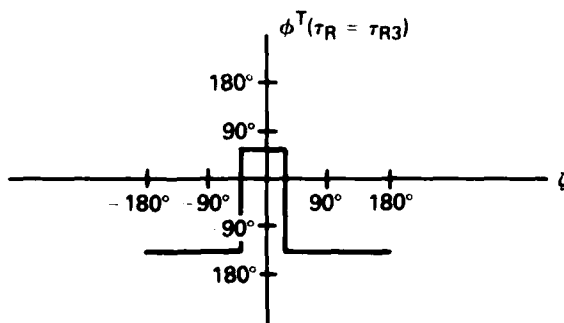


Fig. 19 — Graph of $\phi^T(\tau_{R3})$ versus orbit angle ζ . For this synchronization time the abrupt changes in phase occur around the $\zeta = 0$ point rather than around the $\zeta = 180^\circ$ for the τ_{R2} case illustrated in Fig. 15.

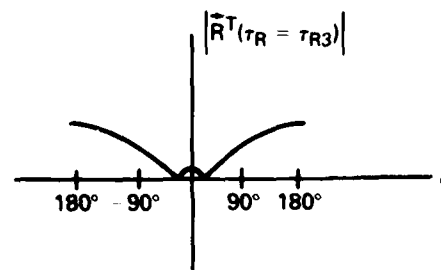


Fig. 20 — Graph of $|\tilde{R}^T(\tau_{R3})|$ versus orbit angle ζ . The smallest values of $|\tilde{R}^T(\tau_{R3})|$ occur for orbit angles near zero degrees rather than near 180° as was the case for $|\tilde{R}^T(\tau_{R2})|$ as shown in Fig. 10.

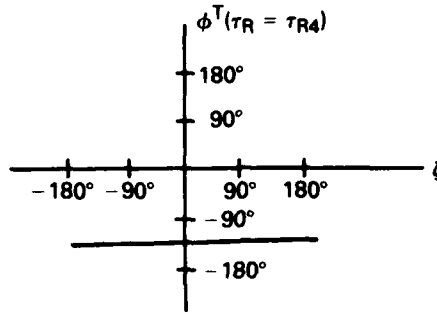


Fig. 21 — Graph of $\phi_I^T(\tau_{R4})$ versus orbit angle ζ . For this receiver time the vertically generated correlation vector dominates; that is $|\bar{R}_I^{ve}(\tau_{R4})| > |\bar{R}_I^{he}(\tau_{R4})|$. No change of phase can occur, since $\bar{R}_I^{ve}(\tau_{R4})$ and $\bar{R}_I^{he}(\tau_{R4})$ are parallel.

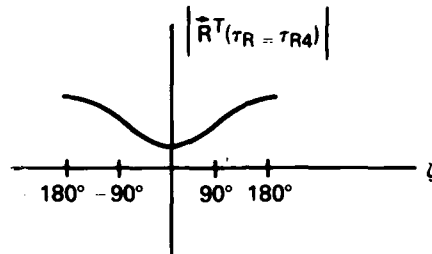


Fig. 22 — Graph of $|\bar{R}_I^T(\tau_{R4})|$ versus orbit angle ζ . For this receiver time the maximum correlation vector occurs for $\zeta = 180^\circ$, whereas for τ_{R1} the maximum correlation-vector magnitude occurred at $\zeta = 0^\circ$.

Finally, Fig. 23 shows an estimate of τ_{Ropt} , the optimum value of receiver correlation time for different values of orbit angle ζ . This graph shows that τ_{R1} and τ_{R4} are preferable when $|\bar{R}_I(\tau_{R1})|$ and $|\bar{R}_I(\tau_{R4})|$ are largest. The phase is constant, and the amplitude varies gently. Relatively mild amplitude behavior occurs for this correlation time because $|\bar{R}_I^{ve}(\tau_{R1})| > |\bar{R}_I^{he}(\tau_{R1})|$. The phase is constant because $\bar{R}_I^{ve}(\tau_{R1})$ is parallel to $\bar{R}_I^{he}(\tau_{R1})$. Although $\bar{R}_I^{ve}(\tau_{R1})$ can change the magnitude of $\bar{R}_I^T(\tau_{R1})$, it does not change the phase.

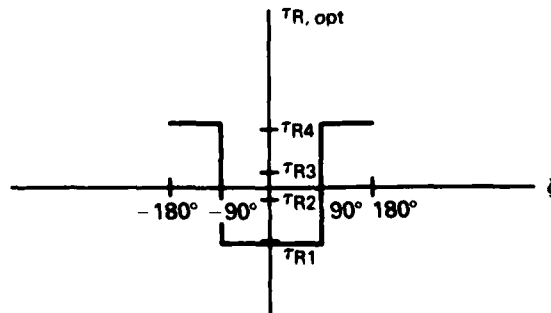


Fig. 23 — Graph showing the values of τ_R that should be chosen for various orbit angles ζ for the case illustrated in Figs. 7 through 22

In the preceding example, there was minimum correlation near the middle of the correlation envelope, and the correlation maximum was greatly displaced from the maximum point of the correlation of either individual multipath signal. Thus, the rather small difference in arrival times $\tau_{p1} - \tau_{p2}$ changes the optimum chip synchronization time τ_R by a major amount. This effect is fairly easy to explain. The condition described by our equations is a severe case of multipath interference. Two signals come to the receiver antenna offset in time by $\tau_{p1} - \tau_{p2}$. The first and second signals travel independently of each other, so when the first signal pulse arrives, the signal begins to build up. Then the second signal arrives out of phase and cancels out the first signal for a long interval of time while both are strong. Then the first signal goes to zero because its waveform has passed by, while the second signal remains to give an excitation of the antenna again. Thus the strongest portions of each signaling element in this case of interference occur at the beginning and the end of each signaling element. In the middle of the element, the two signals arriving from different paths interfere, and there is a reduction of the field present.

When a receiver tries to synchronize with the signal at its strongest point, it must search for synchronization either at the beginning of the chip or at the end but not in the middle. Thus, if a system were presynchronized with an optimum τ_R for either of the individual mode delays or for an average of the two mode delays, it would actually be poorly synchronized for optimum operation! For better operation three correlators might be used—one adjusted at the central expected time of arrival of the wave, and one at each end of the chip. If the two waveforms reinforce each other to give the maximum in the middle, the central correlation peak will be large and the two side peaks will be small. If however, an interference condition is present, the middle correlator will be weak and the two side correlators will be strong.

NUMERICAL CALCULATIONS

Procedures

We will calculate some values of \bar{R}_I^T for cases that are inspired by realistic mode-theory calculations of the phase and amplitude of VLF waves. For the calculated fields shown in Fig. 6, the waveguide mode constants are given in Table 1.

Table 1 — Constants Used in the Calculations

$\Lambda_1 = 0.4$	$G_1(z) = 1$
$\Lambda_2 = 1.2$	$G_2(z) = 1$
$S_1 = 1.002 + 0.000689i$	$\Delta_1(z_s) = -0.02i$
$S_2 = 0.003 + 0.00138i$	$\Delta_2(z_s) = 0.05i$
$z = 0 \text{ km}$	$r_0 = 4 \text{ km}$
$G_1(z_s) = 0.965 + 0.259i$	$z_s = 10 \text{ km}$
$G_2(z_s) = 0.95$	Radiated power = 1 kw

These constants were used in the following equations to generate the field strength values in Fig. 6:

$$E_r^{ve}(r, \theta) = i(\mu_0/\epsilon_0)^{1/2} \int ds^{ve} \sum_n S_n^{1.5} F_n \quad (57)$$

and

$$E_r^{he}(r, \theta) = i(\mu_0/\epsilon)^{1/2} \int ds^{he} \cos \phi \sum_n \Delta_n(z_s) S_n^{0.5} F_n \quad (58)$$

where

$$F_n = \frac{1}{(D\lambda h)^{1/2}} \left[\frac{D/a}{\sin(D/a)} \right]^{1/2} G_n(z) G_n(z_s) \Lambda_n \exp(i\pi/4 + ik_0 DS_n). \quad (59)$$

These equations are simplified versions of Eqs. (51) through (53), since they contain only TM-mode constants of an isotropic ionosphere. We calculate $\bar{R}_i^{(i)ve}$ for each mode according to

$$X_i^{(i)ve}(\tau_R, \zeta) = N |A_i^{ve}| \cos[\omega_0 \tau_i^{ve}(\zeta)] C(\tau_i^{ve}(\zeta) - \tau_R) \quad (60)$$

and

$$Y_i^{(i)ve}(\tau_R, \zeta) = N |A_i^{ve}| \sin[\omega_0 \tau_i^{ve}(\zeta)] C(\tau_i^{ve}(\zeta) - \tau_R), \quad (61)$$

where

- N is a normalizing constant,
- A_i^{ve} is amplitude of the i th TM mode generated by the vertical component of the transmitting antenna,
- ω_0 is the angular frequency of the wave,
- $\tau_i^{ve}(\zeta)$ is the delay time of the phase of the wave when the aircraft is at angle ζ of its orbit for the i th waveguide mode, and
- $\tau_i^{ve}(\zeta)$ is the group delay time of the wave when the aircraft is at angle ζ of its orbit for the i th waveguide mode.

The amplitude is given by

$$A_i^{ve} = S_i^{1.5} G_i(z) G_i(z_s) \Lambda_i \exp(i\pi/r + i k_0 D S_i). \quad (62)$$

The phase delay time $\tau_i^{ve}(\zeta)$ is obtained by evaluating the phase of A_i :

$$\omega_0 \tau_i^{ve}(\zeta) = \arg(A_i^{ve}). \quad (63)$$

The group delay time $\tau_i^{ve}(\zeta)$ is obtained by evaluating the derivative of the phase of A_i :

$$\tau_i^{ve}(\zeta) = \frac{\partial}{\partial \omega} [\arg(A_i^{ve})]. \quad (64)$$

The path length D from the transmitting antenna to the receiver location is a function of the orbit angle ζ and the orbit radius r according to the approximation

$$D = D_0 + r \sin \zeta, \quad (65)$$

where D_0 is the distance from the receiver to the center of the orbit. To calculate $\bar{R}_i^{ve}(\zeta, \tau_R)$, we performed summations as indicated in Eqs. (54) through (56).

We calculate the horizontally electrically generated fields in an analogous manner:

$$X_i^{(i)he}(\tau_R, \zeta) = N |A_i^{he}| \cos[\omega_0 \tau_i^{he}(\zeta)] C_0(\tau_i^{he}(\zeta) - \tau_R) \quad (66)$$

and

$$Y_i^{(i)he}(\tau_R, \zeta) = N |A_i^{he}| \sin[\omega_0 \tau_i^{he}(\zeta)] C_0(\tau_i^{he}(\zeta) - \tau_R). \quad (67)$$

The amplitude of the i th mode is given as follows:

$$A_i^{he} = G_i(z) G_i(z_s) \Lambda_i \exp(i\pi/4 + i k_0 D S_i) S_i^{1.5} \Delta_i(z_s) = A_i^{ve} S_i \Delta_i(z_0). \quad (68)$$

The phase and group delay times are given in the same manner as for the vertically generated modes:

$$\omega_0 \tau_i^{he}(\zeta) = \arg(A_i^{he}) \quad (69)$$

and

$$\tau_{f,he}(\zeta) = \frac{\partial}{\partial \omega} [\arg(A_{f,he})]. \quad (64)$$

Tables 2 and 3 give the numerical values used in making the correlation calculations.

Table 2 — Set of Quantities Used in Calculation of Correlation Vectors

Mode	Quantity	Value
1	$ A_1^{ve} $	$1.26500262 \times 10^{-1}$
	$\tau_{f,ve}$	$1.33658211 \times 10^{-2}$
	$\tau_{f,ve}$	1.34400×10^{-2}
	$ A_1^{he} $	$2.52495471 \times 10^{-3}$
	$\tau_{f,he}$	$1.33533157 \times 10^{-2}$
	$\tau_{f,he}$	1.34400×10^{-2}
2	$ A_2^{ve} $	$1.11773228 \times 10^{-1}$
	$\tau_{f,ve}$	$1.32437617 \times 10^{-2}$
	$\tau_{f,ve}$	1.356666×10^{-2}
	$ A_2^{he} $	$5.62805237 \times 10^{-3}$
	$\tau_{f,he}$	$1.32562578 \times 10^{-2}$
	$\tau_{f,he}$	1.356666×10^{-2}

Table 3 — Second Set of Quantities Used in Calculation of Correlation Vectors

Mode	Quantity	Value
1	$ A_1^{ve} $	$1.26500262 \times 10^{-1}$
	$\tau_{f,ve}$	$1.33658211 \times 10^{-2}$
	$\tau_{f,ve}$	1.34400×10^{-2}
	$ A_1^{he} $	$2.52495471 \times 10^{-3}$
	$\tau_{f,he}$	1.3315820×10^{-2}
	$\tau_{f,he}$	1.34400×10^{-2}
2	$ A_2^{ve} $	$1.26500262 \times 10^{-1}$
	$\tau_{f,ve}$	$1.33908211 \times 10^{-2}$
	$\tau_{f,ve}$	1.356666×10^{-2}
	$ A_2^{he} $	$5.62805237 \times 10^{-3}$
	$\tau_{f,he}$	1.3365820×10^{-2}
	$\tau_{f,he}$	1.356666×10^{-2}

Results

Figures 24 through 29 show $\bar{R}_I^T(\tau_R)$ and $\phi_I^T(\tau_R)$ contours for γ values of 90°, 85°, 80°, 60°, 45°, and 0° with the propagation parameters of Table 2. Figure 30 shows $\bar{R}^{(1)ve}(\tau_R)$, the correlation vector of the first-order mode. Figures 31 through 36 show the correlation vector for propagation parameters of Table 3 for γ values of 90°, 85°, 80°, 60°, 45°, and 0°. The "average" chip duration for each of these calculations was $\tau_c = 1$ ms. The total length of each chip is $T = 2\tau_c = 2$ ms. The radius of the orbit is 3 km; the distance from the center of the orbit to the receiver is 4000 km.

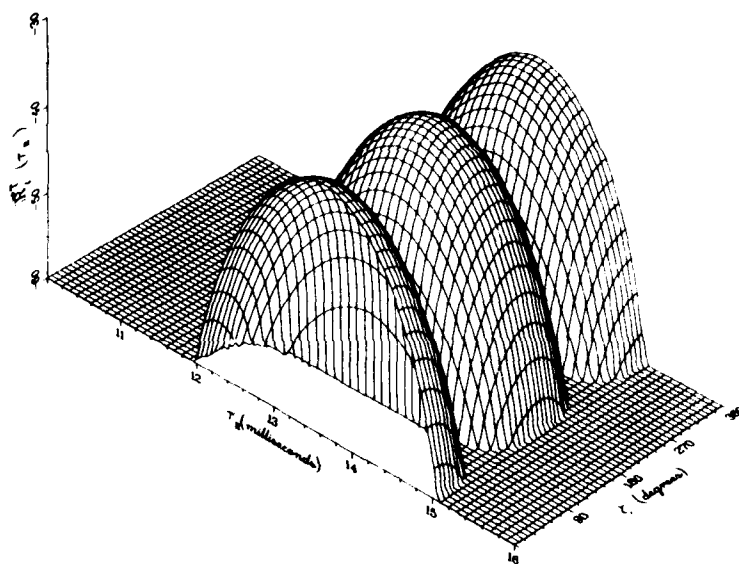


Fig. 24a — Amplitude behavior of $\bar{R}_I^T(t_R)$ for $\gamma = 90^\circ$, calculated with the parameters of Table 2

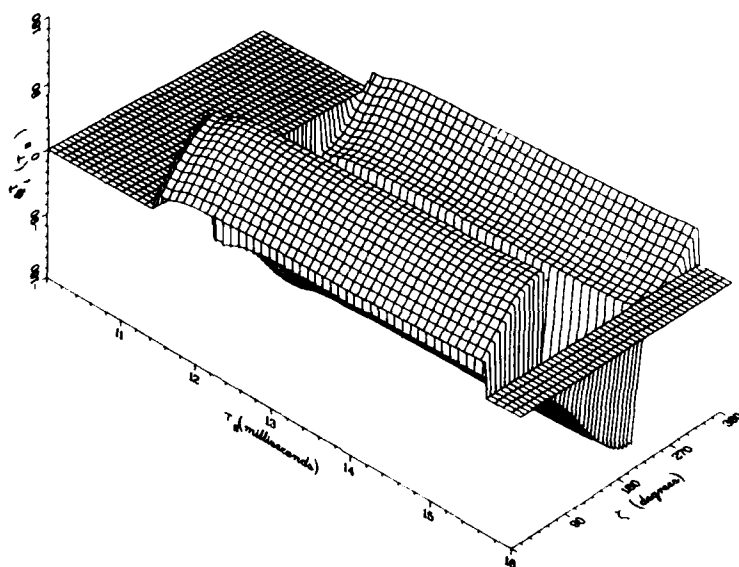


Fig. 24b — Phase behavior of $\bar{R}_I^T(t_R)$ for $\gamma = 90^\circ$, calculated with the parameters of Table 2

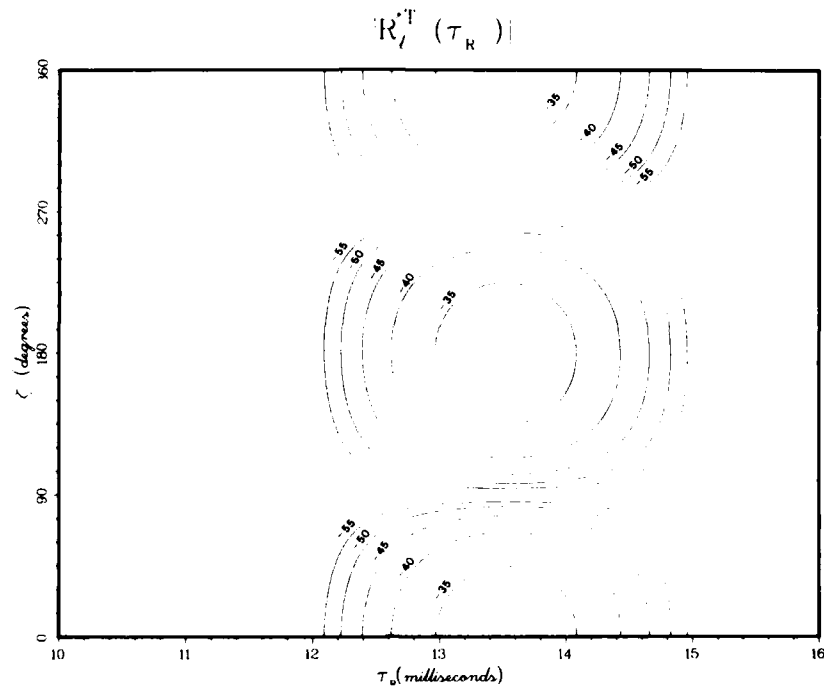


Fig. 24c — Amplitude contours corresponding to Fig. 24a

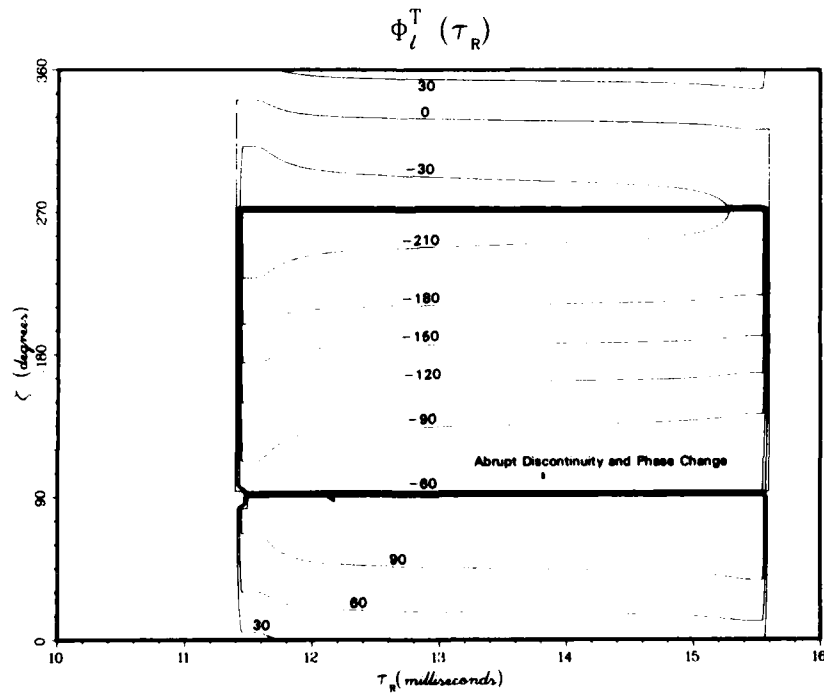


Fig. 24d — Phase behavior corresponding to Fig. 24b

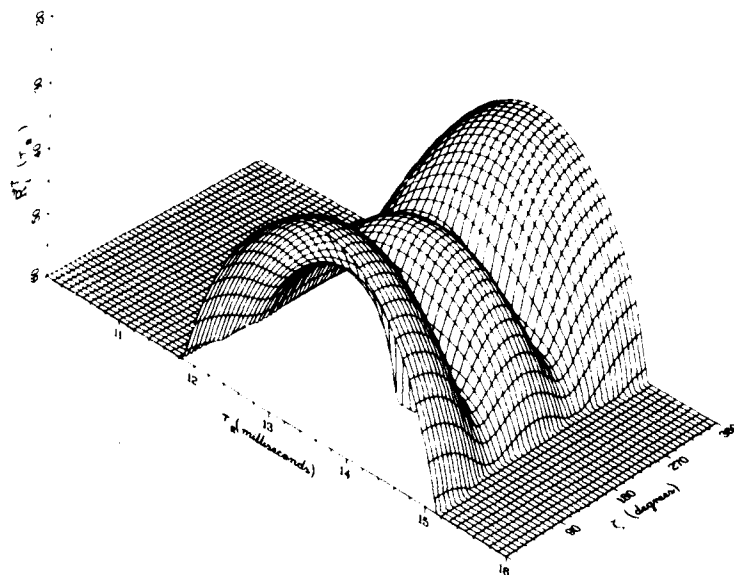


Fig. 25a Amplitude behavior of $\bar{R}_I^T(\tau_R)$ for $\gamma = 85^\circ$, calculated with the parameters of Table 2

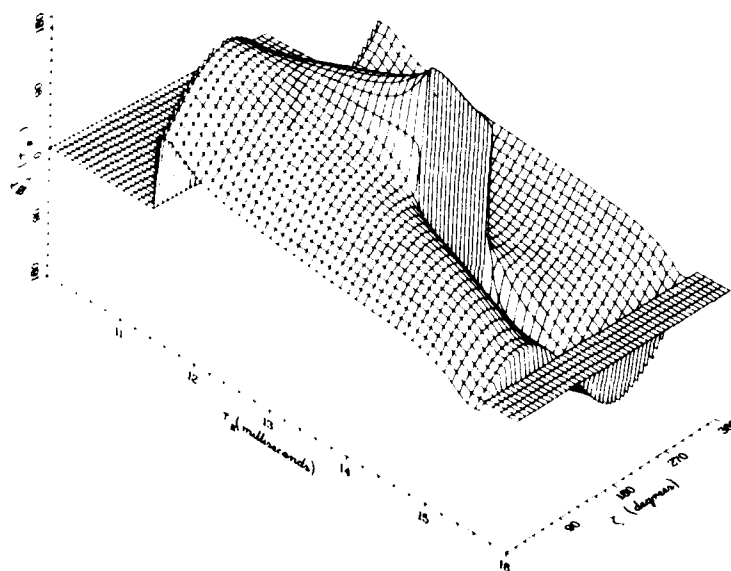


Fig. 25b — Phase behavior of $\bar{R}_I^T(\tau_R)$ for $\gamma = 85^\circ$, calculated with the parameters of Table 2

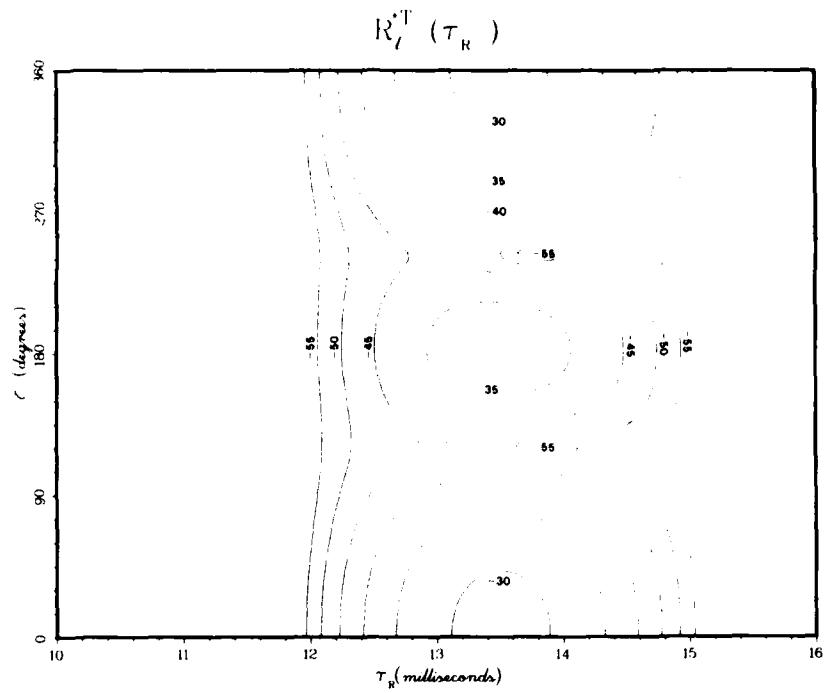


Fig. 25c — Amplitude contours corresponding to Fig. 25a

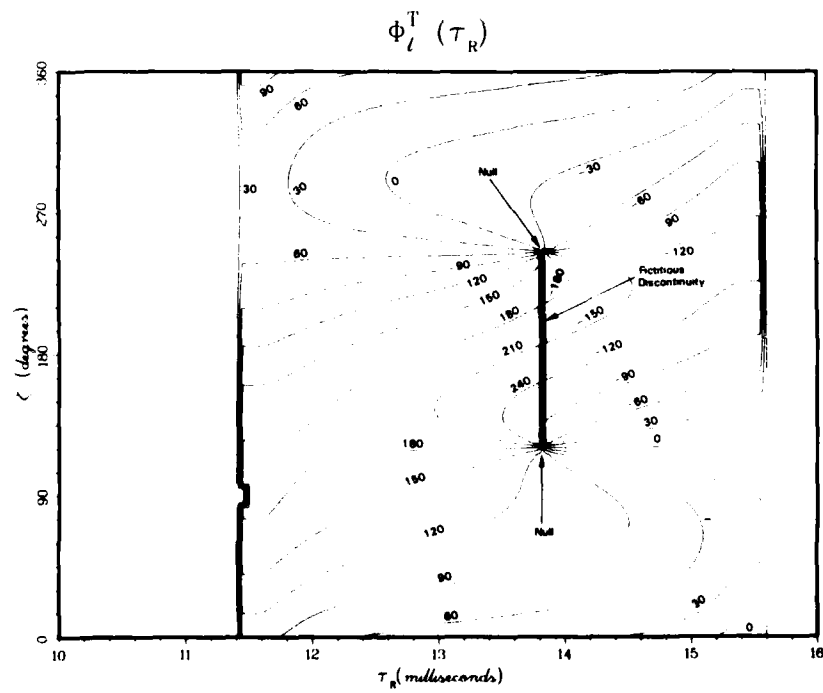


Fig. 25d — Phase behavior corresponding to Fig. 25b

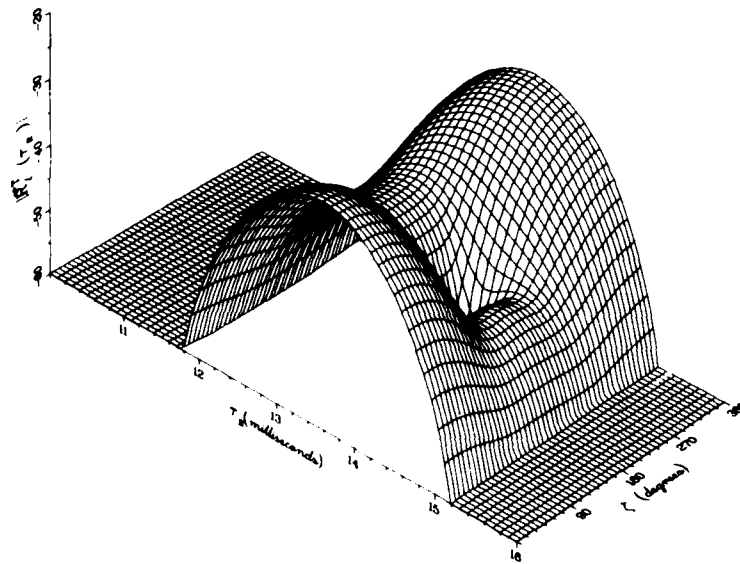


Fig. 26a — Amplitude behavior of $\bar{R}_l^T(r_R)$ for $\gamma = 80^\circ$, calculated with the parameters of Table 2

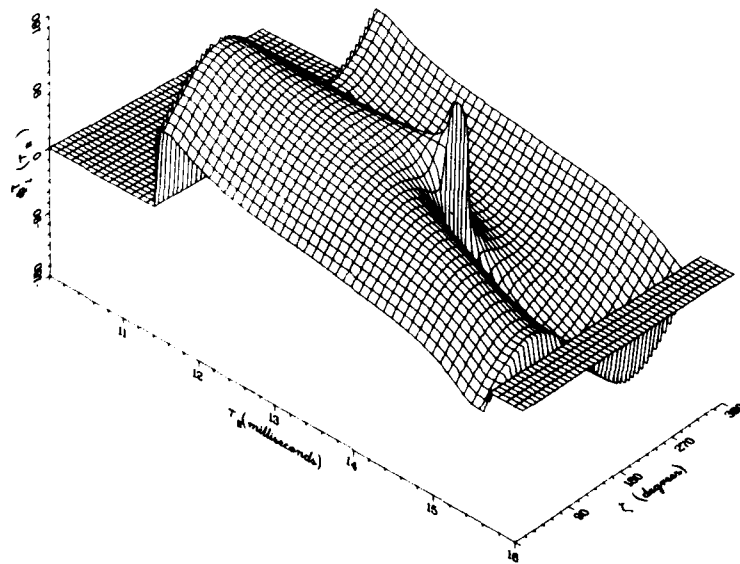


Fig. 26b — Phase behavior of $\bar{R}_l^T(r_R)$ for $\gamma = 80^\circ$, calculated with the parameters of Table 2

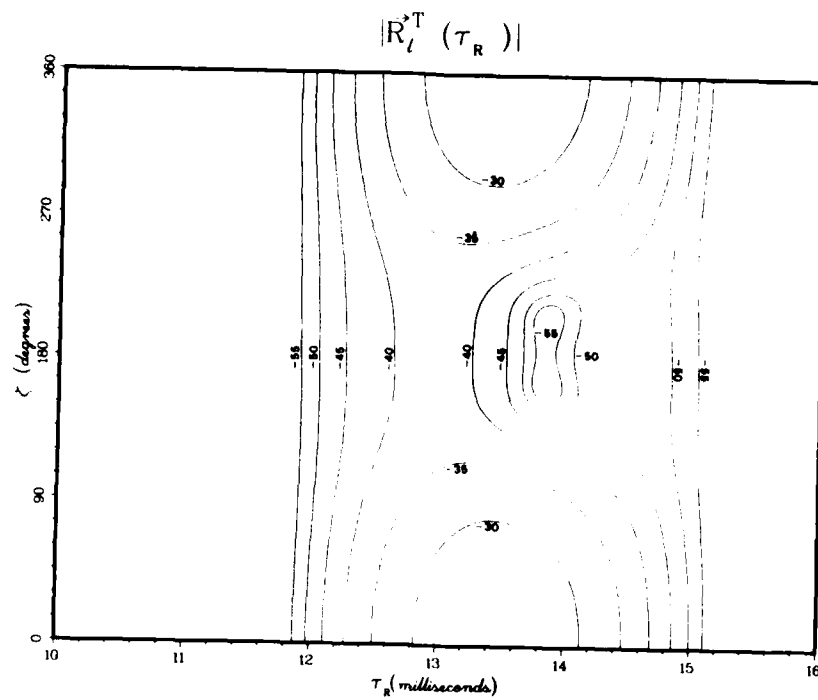


Fig. 26c — Amplitude contours corresponding to Fig. 26a

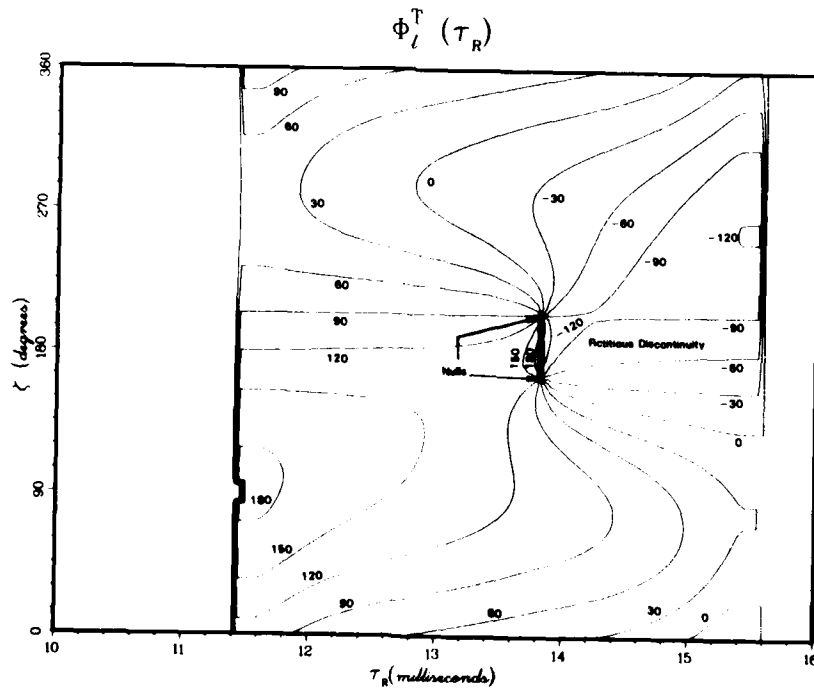


Fig. 26d — Phase behavior corresponding to Fig. 26b

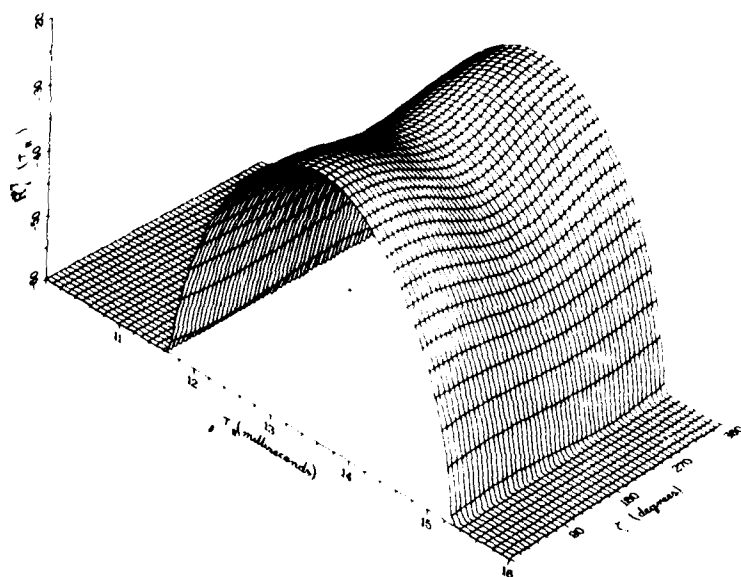


Fig. 27a — Amplitude behavior of $\bar{R}_I^T(\tau_R)$ for $\gamma = 60^\circ$, calculated with the parameters of Table 2

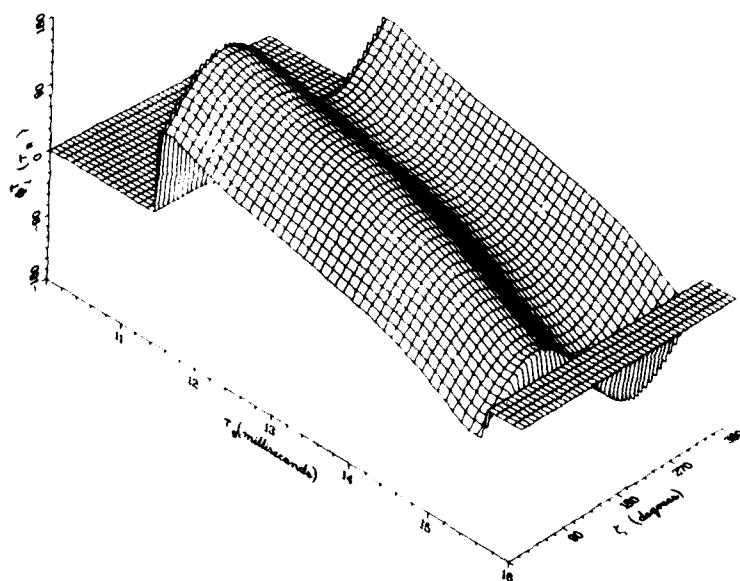


Fig. 27b — Phase behavior of $\bar{R}_I^T(\tau_R)$ for $\gamma = 60^\circ$, calculated with the parameters of Table 2

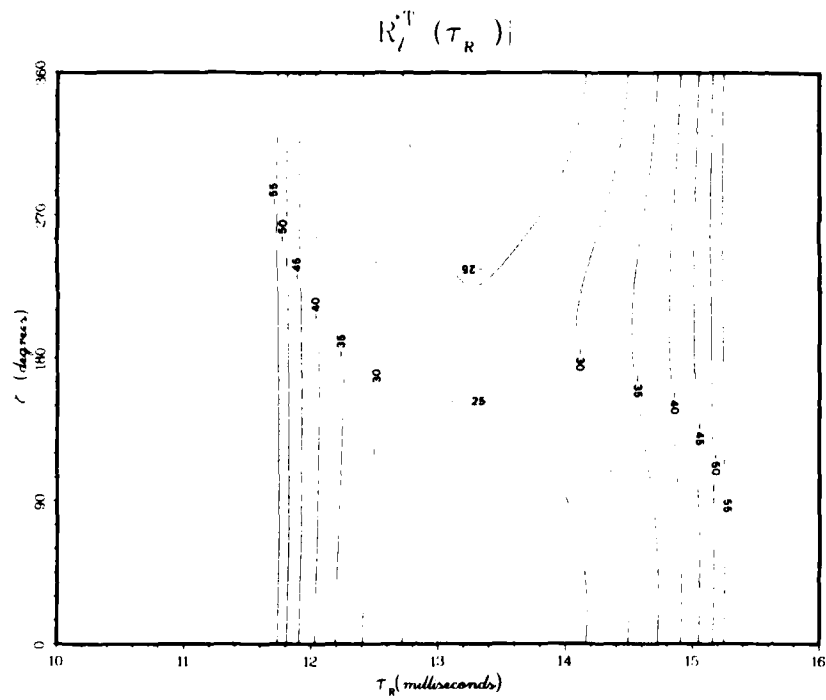


Fig. 27c — Amplitude contours corresponding to Fig. 27a

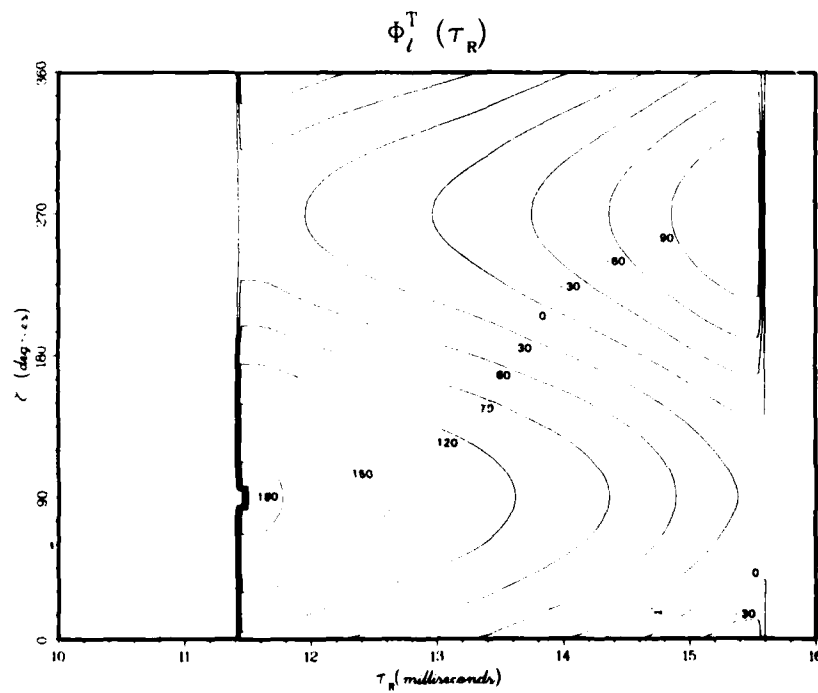


Fig. 27d — Phase behavior corresponding to Fig. 27b

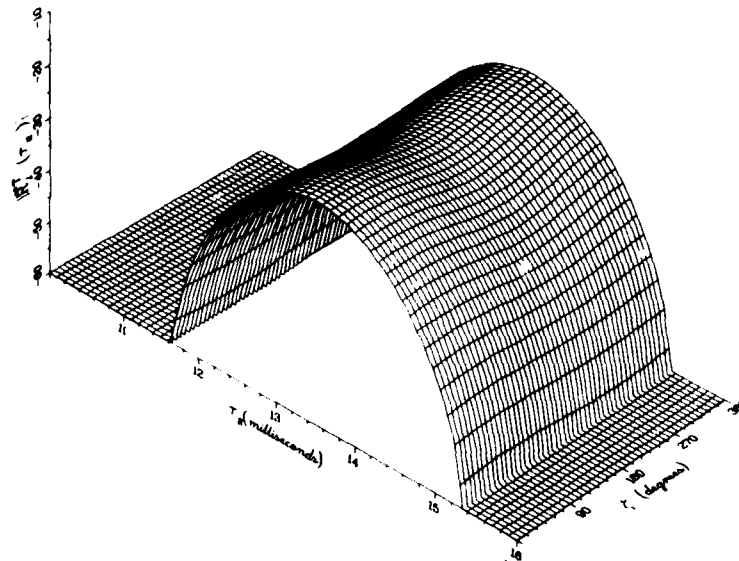


Fig. 28a — Amplitude behavior of $\bar{R}_T(t_R)$ for $\gamma = 45^\circ$, calculated with the parameters of Table 2

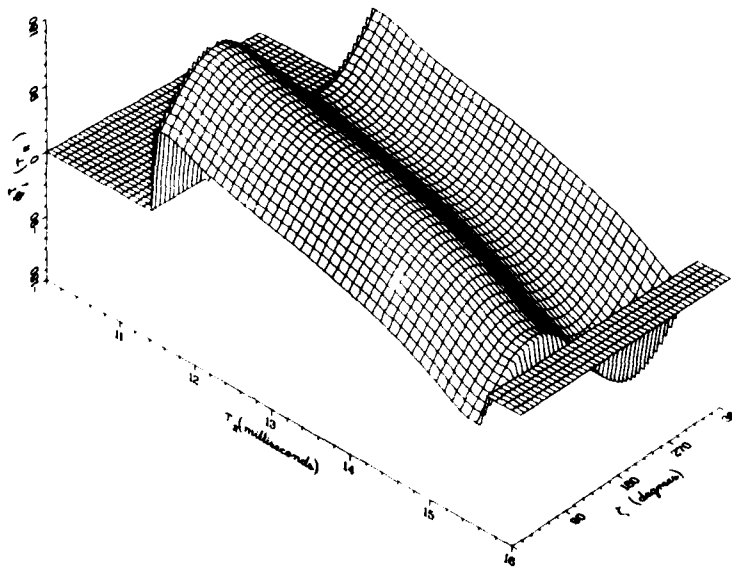


Fig. 28b — Phase behavior of $\bar{R}_T(t_R)$ for $\gamma = 45^\circ$, calculated with the parameters of Table 2

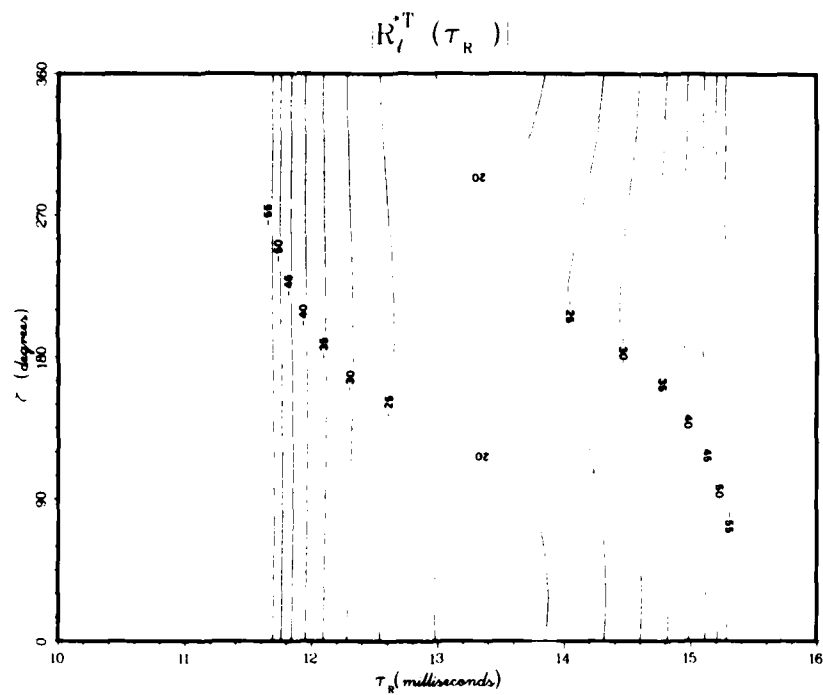


Fig. 28c — Amplitude contours corresponding to Fig. 28a

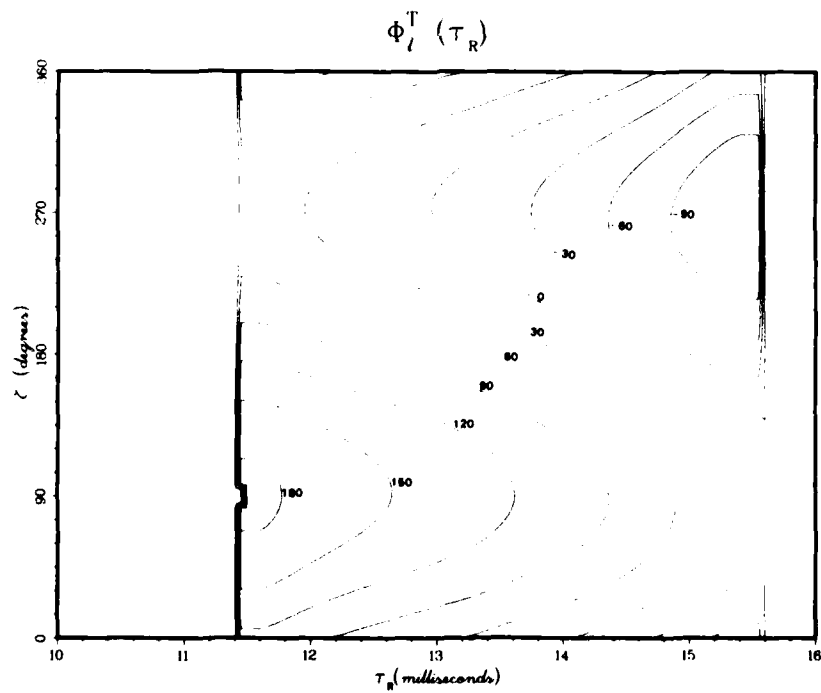


Fig. 28d — Phase behavior corresponding to Fig. 28a

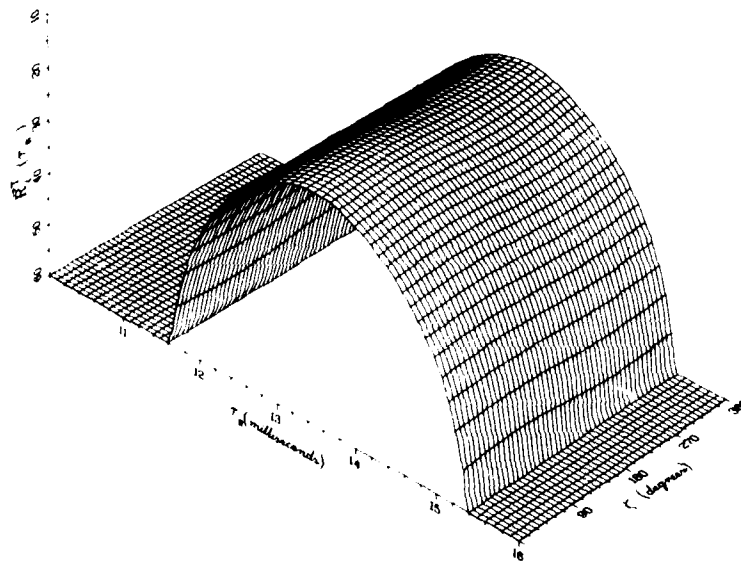


Fig. 29a — Amplitude behavior of $\bar{R}_I^T(t_R)$ for $\gamma = 0^\circ$, calculated with the parameters of Table 2

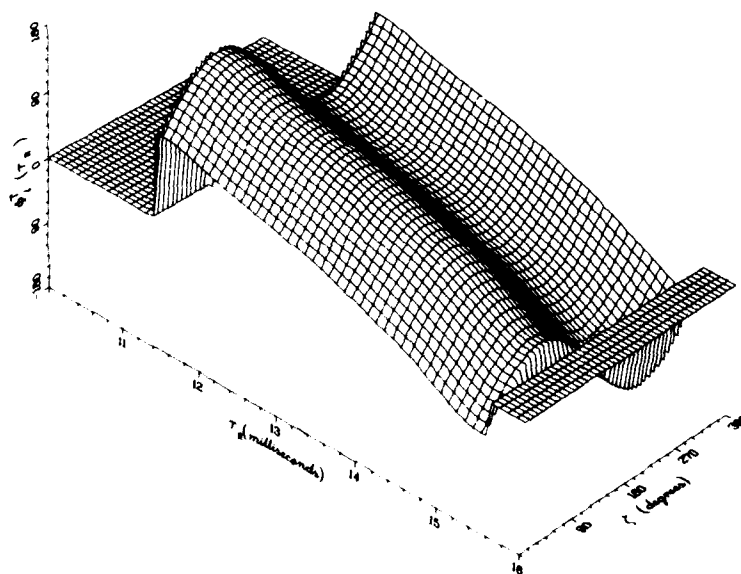


Fig. 29b — Phase behavior of $\bar{R}_I^T(t_R)$ for $\gamma = 0^\circ$, calculated with the parameters of Table 2

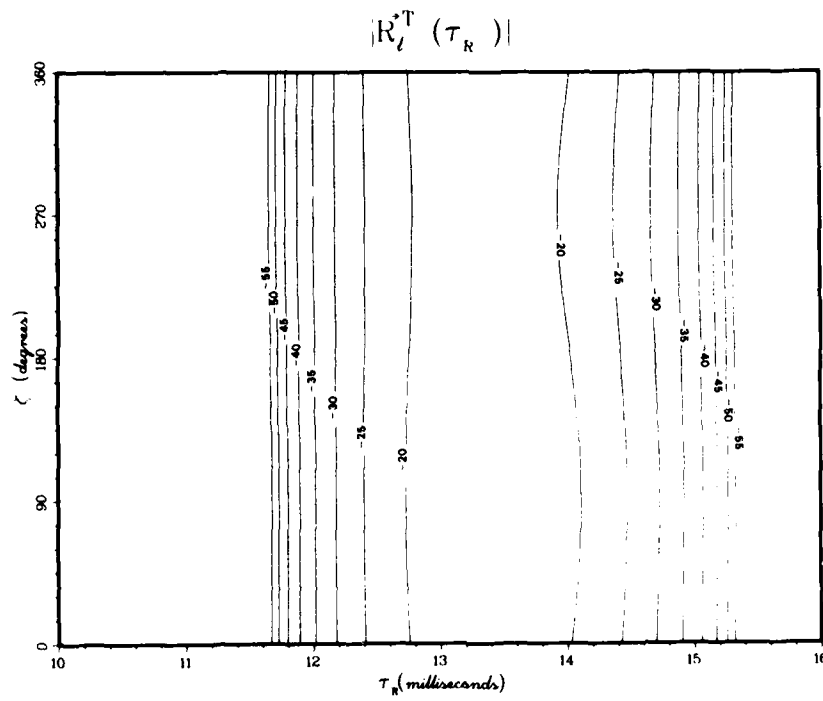


Fig. 29c — Amplitude contours corresponding to Fig. 29a

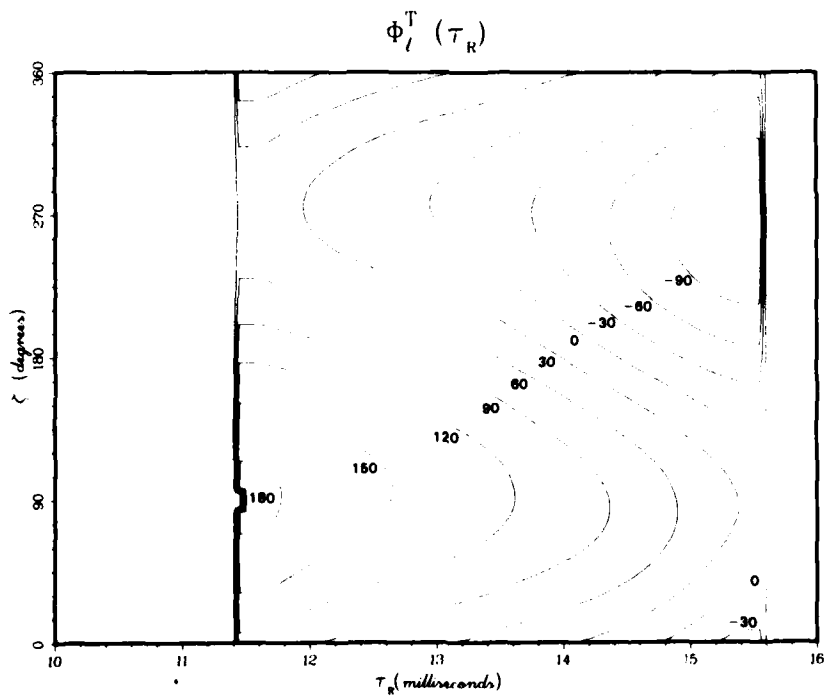


Fig. 29d — Phase behavior corresponding to Fig. 29b

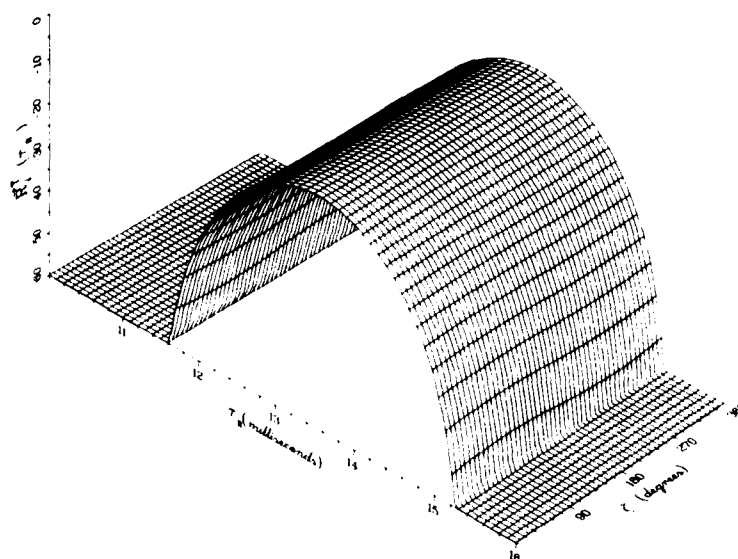


Fig. 30a — Amplitude behavior of $\bar{R}_l^{(1)}(\tau_R)$ for $\gamma = 0^\circ$,
calculated with the parameters of Table 2

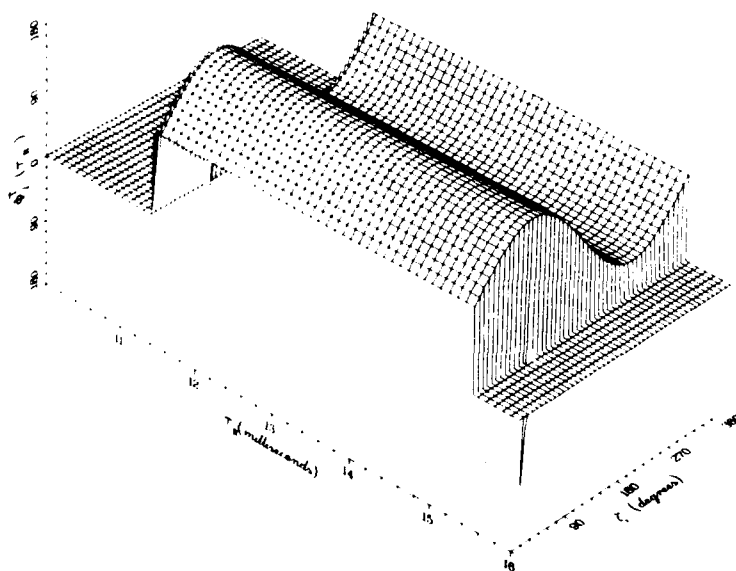


Fig. 30b — Phase behavior of $\bar{R}_l^{(1)}(\tau_R)$ for $\gamma = 0^\circ$,
calculated with the parameters of Table 2

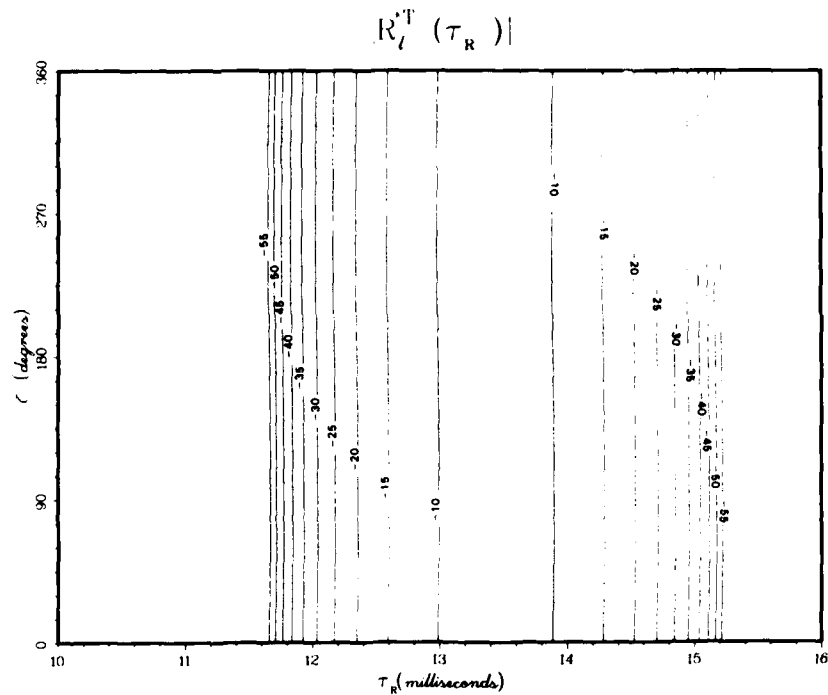


Fig. 30c — Amplitude contours corresponding to Fig. 30a

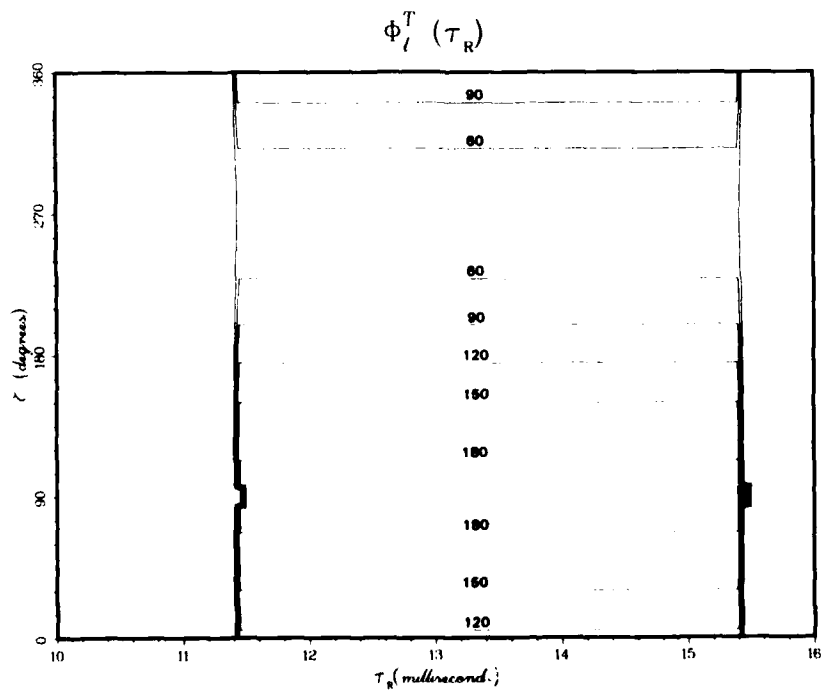


Fig. 30d — Phase behavior corresponding to Fig. 30b

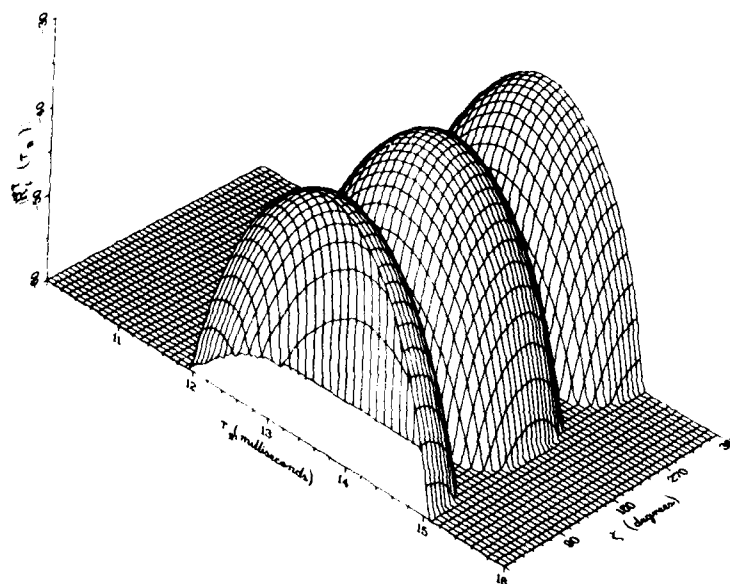


Fig. 31a — Amplitude behavior of $\bar{R}_I^T(\tau_R)$ for $\gamma = 90^\circ$, calculated with the parameters of Table 3

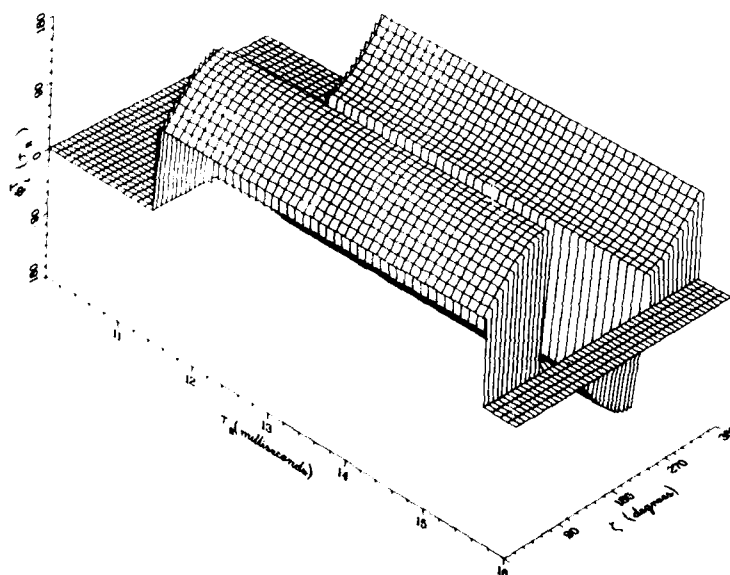


Fig. 31b — Phase behavior of $\bar{R}_I^T(\tau_R)$ for $\gamma = 90^\circ$, calculated with the parameters of Table 3

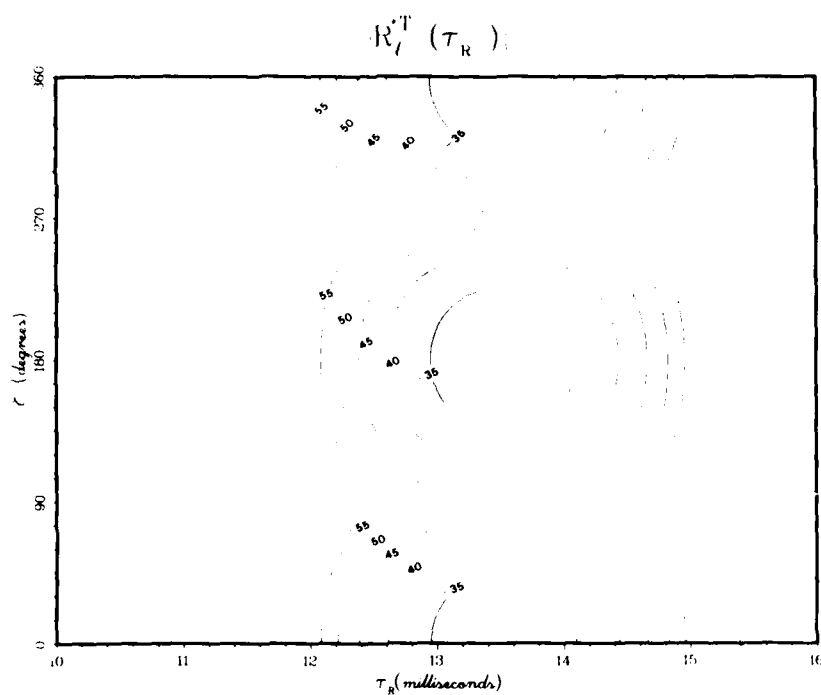


Fig. 31c — Amplitude contours corresponding to Fig. 31a

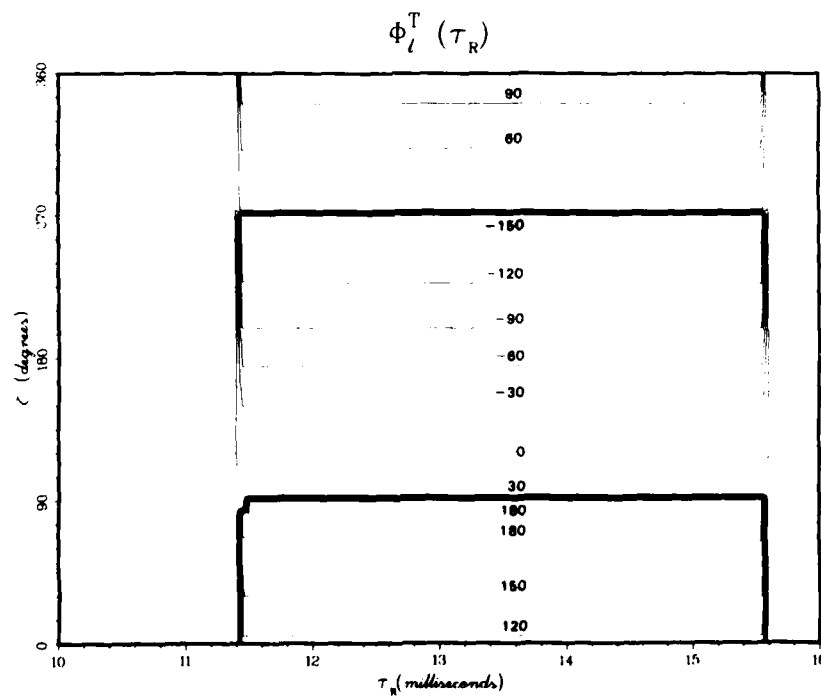


Fig. 31d — Phase behavior corresponding to Fig. 31b

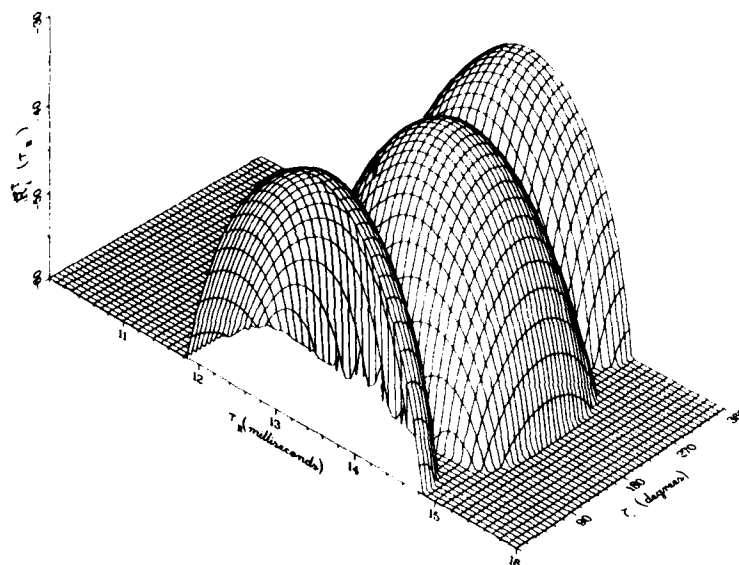


Fig. 32a — Amplitude behavior of $\bar{R}_I^T(t_R)$ for $\gamma = 85^\circ$, calculated with the parameters of Table 3

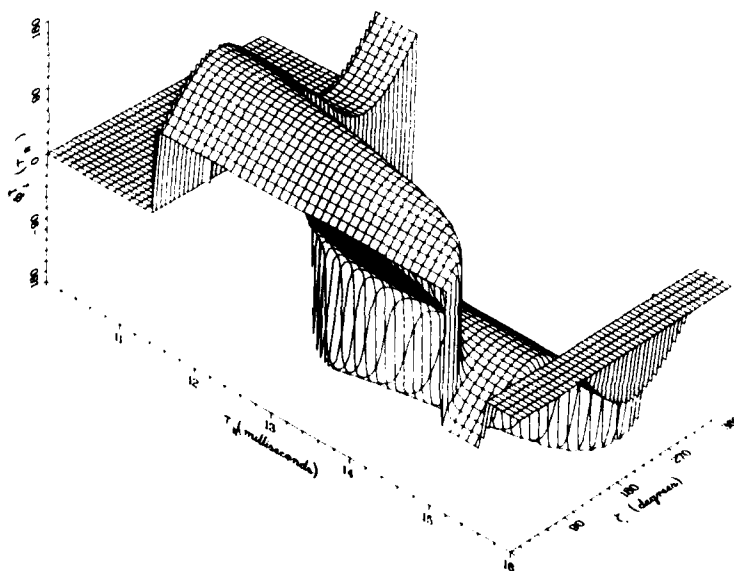


Fig. 32b — Phase behavior of $\bar{R}_I^T(t_R)$ for $\gamma = 85^\circ$, calculated with the parameters of Table 3

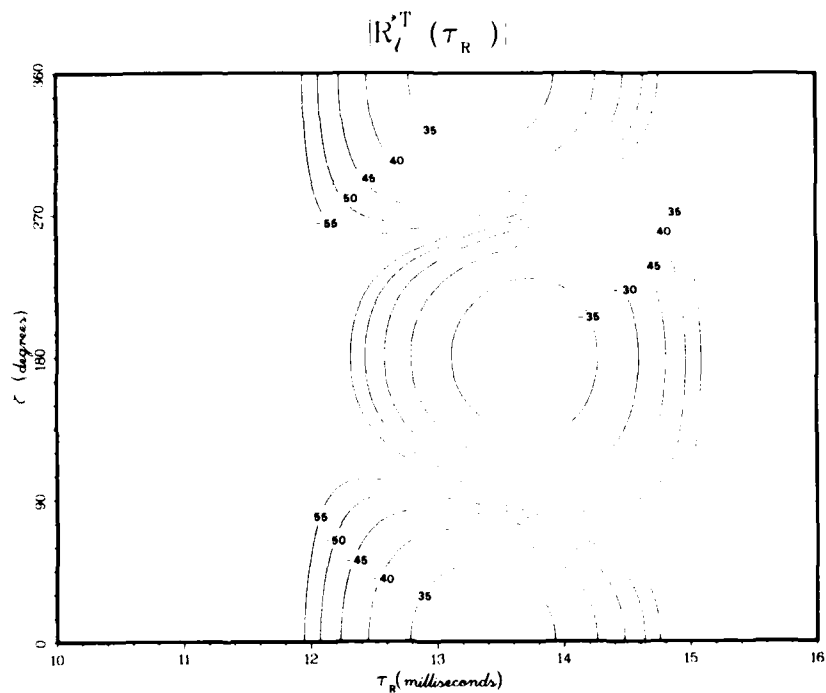


Fig. 32c — Amplitude contours corresponding to Fig. 32a

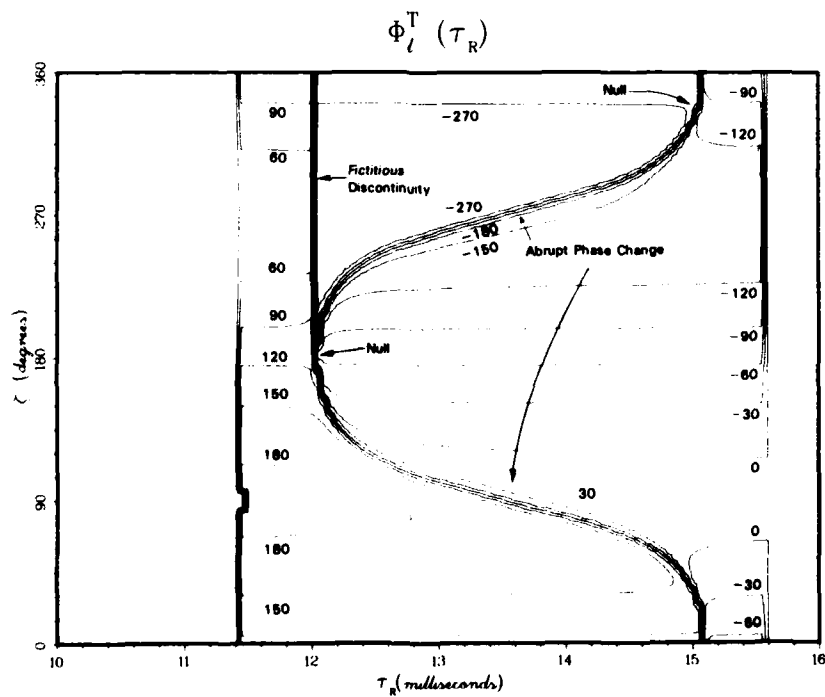


Fig. 32d — Phase behavior corresponding to Fig. 32b

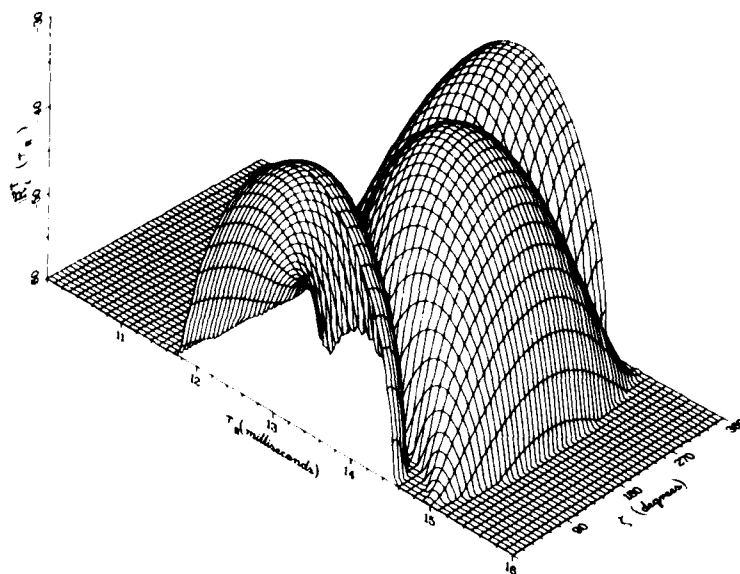


Fig. 33a — Amplitude behavior of $\bar{R}_I^T(t_R)$ for $\gamma = 80^\circ$, calculated with the parameters of Table 3

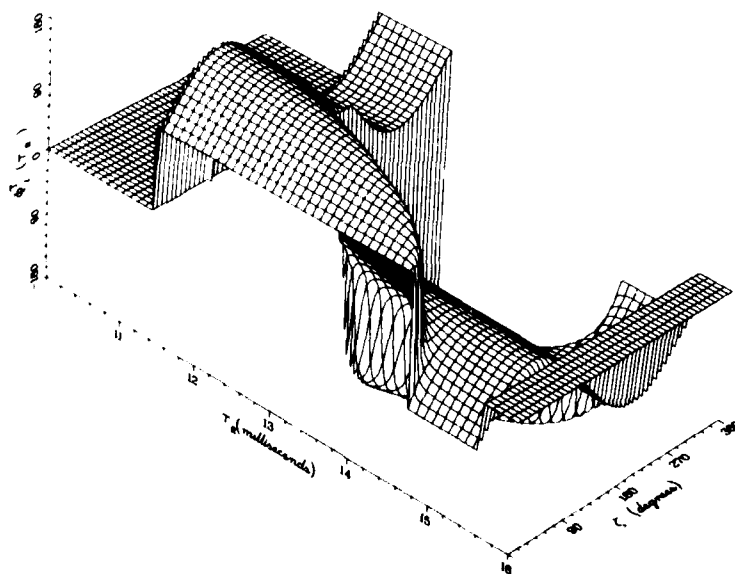


Fig. 33b — Phase behavior of $\bar{R}_I^T(t_R)$ for $\gamma = 80^\circ$, calculated with the parameters of Table 3

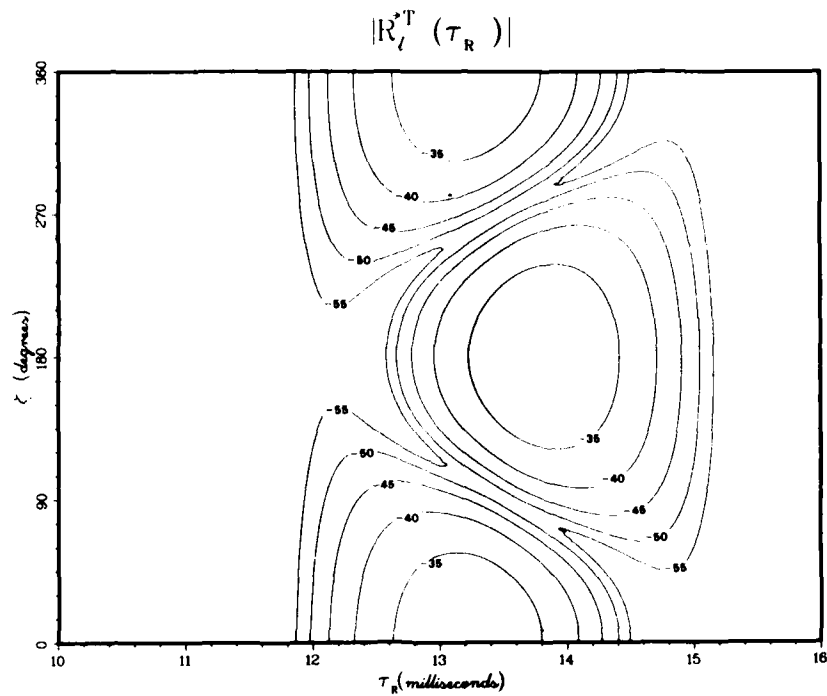


Fig. 33c — Amplitude contours corresponding to Fig. 33a

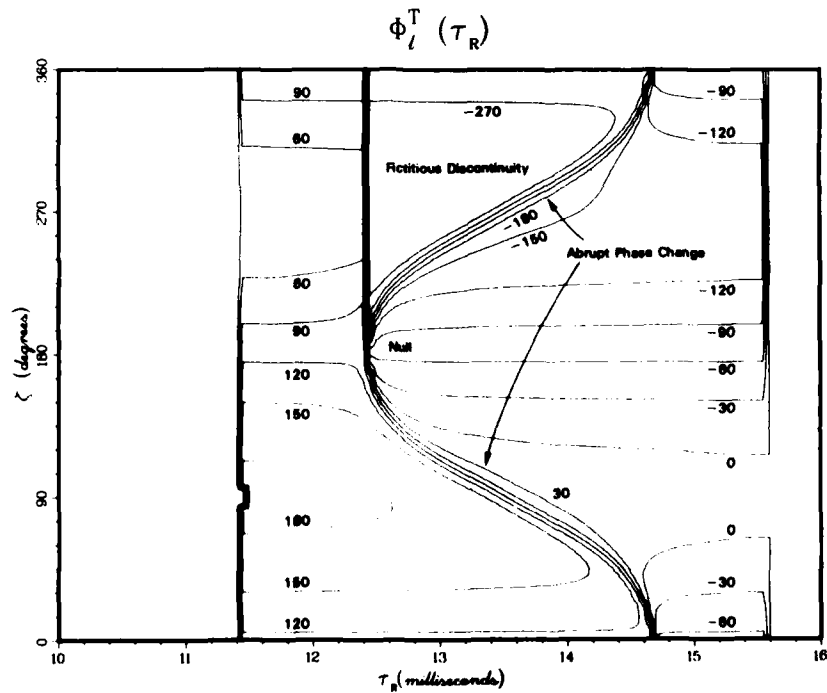


Fig. 33d — Phase behavior corresponding to Fig. 33b

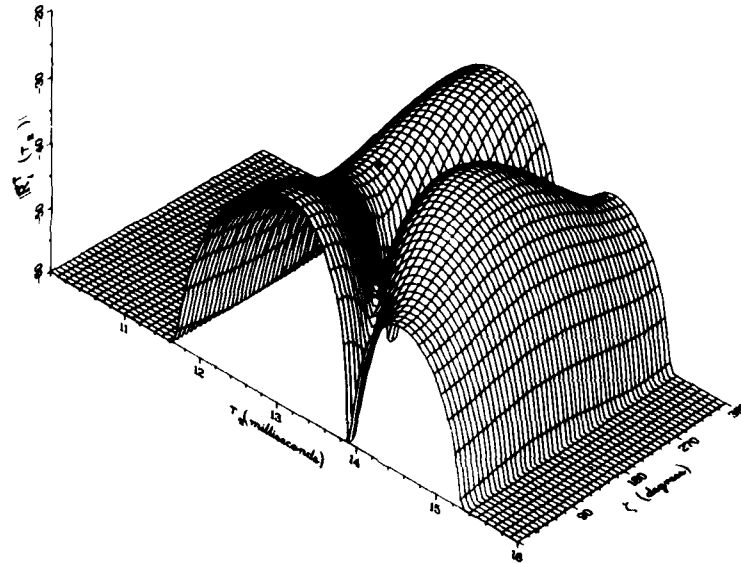


Fig. 34a — Amplitude behavior of $\bar{R}_l^T(t_R)$ for $\gamma = 60^\circ$, calculated with the parameters of Table 3

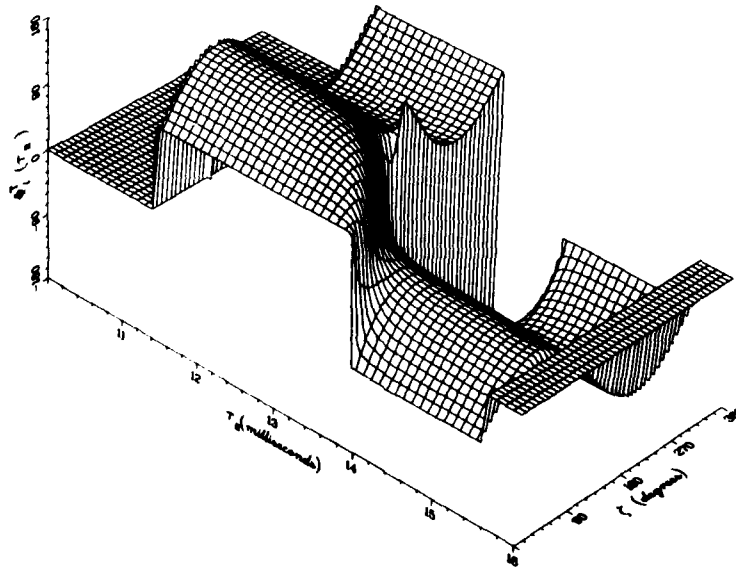


Fig. 34b — Phase behavior of $\bar{R}_l^T(t_R)$ for $\gamma = 60^\circ$, calculated with the parameters of Table 3

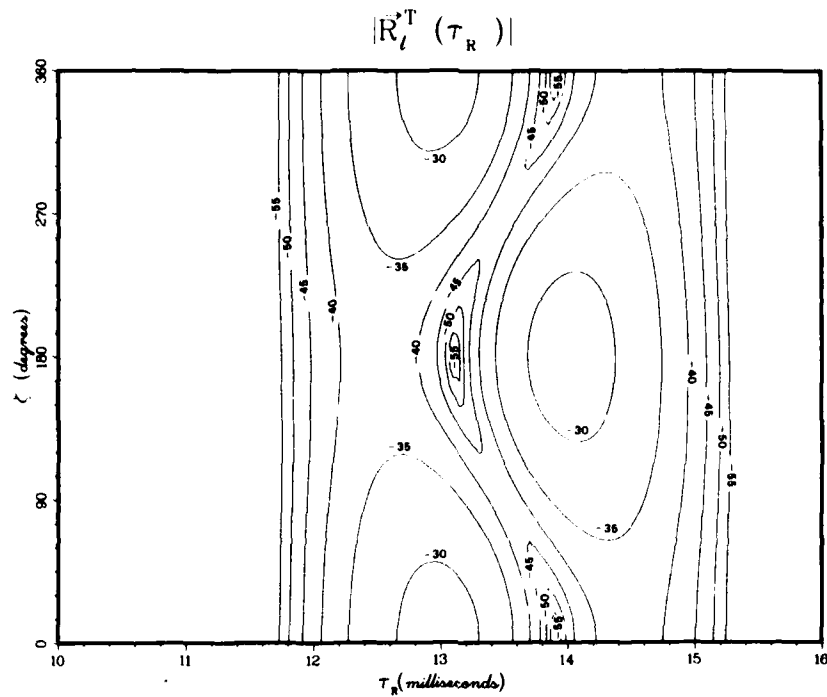


Fig. 34c — Amplitude contours corresponding to Fig. 34a

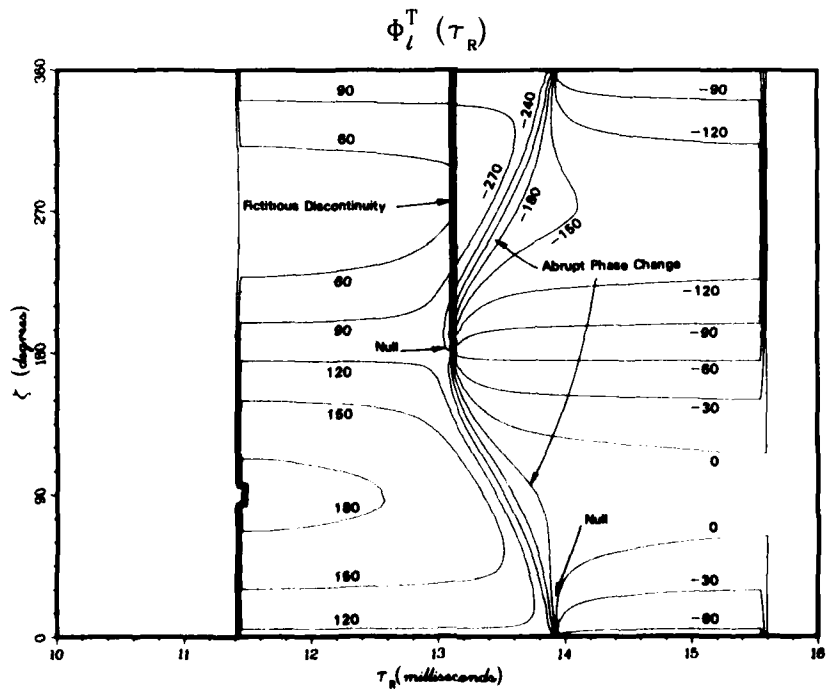


Fig. 34d — Phase behavior corresponding to Fig. 34b

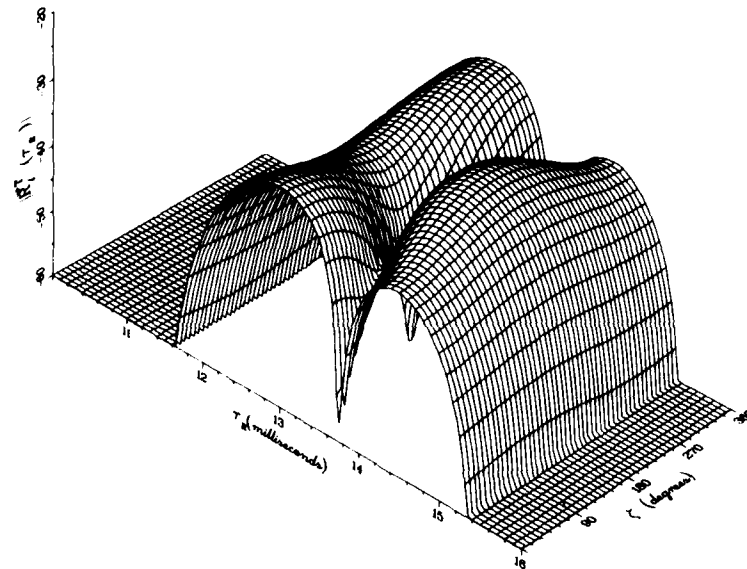


Fig. 35a — Amplitude behavior of $\bar{R}_I^T(\tau_R)$ for $\gamma = 45^\circ$,
calculated with the parameters of Table 3

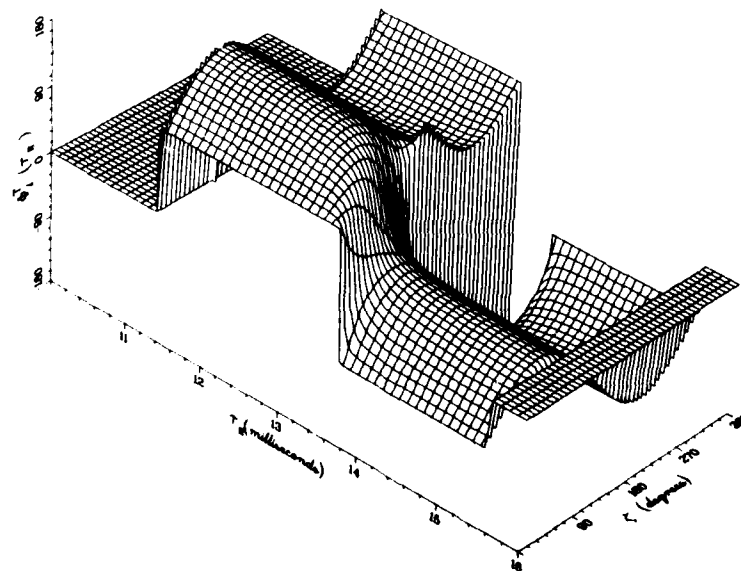


Fig. 35b — Phase behavior of $\bar{R}_I^T(\tau_R)$ for $\gamma = 45^\circ$,
calculated with the parameters of Table 3

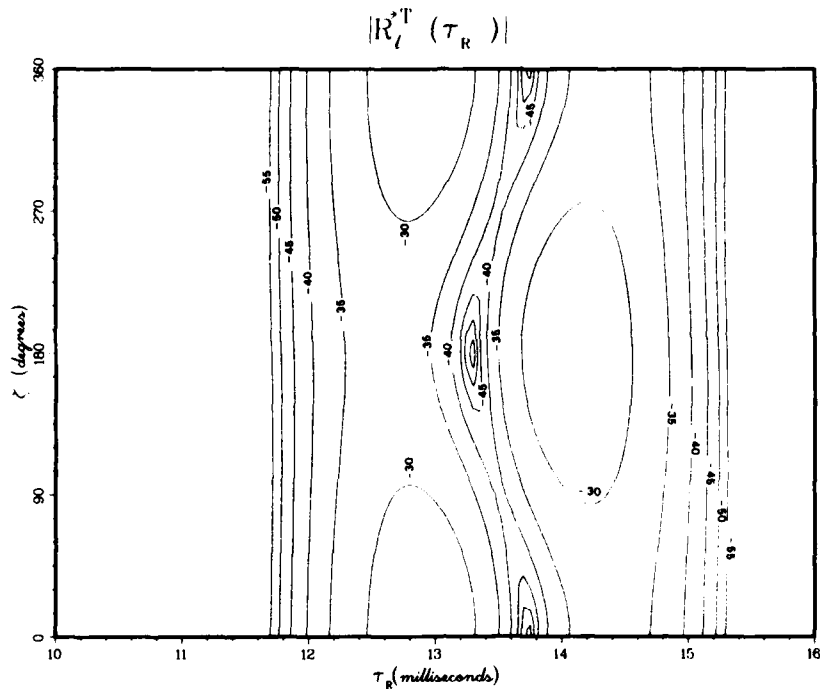


Fig. 35c — Amplitude contours corresponding to Fig. 35a

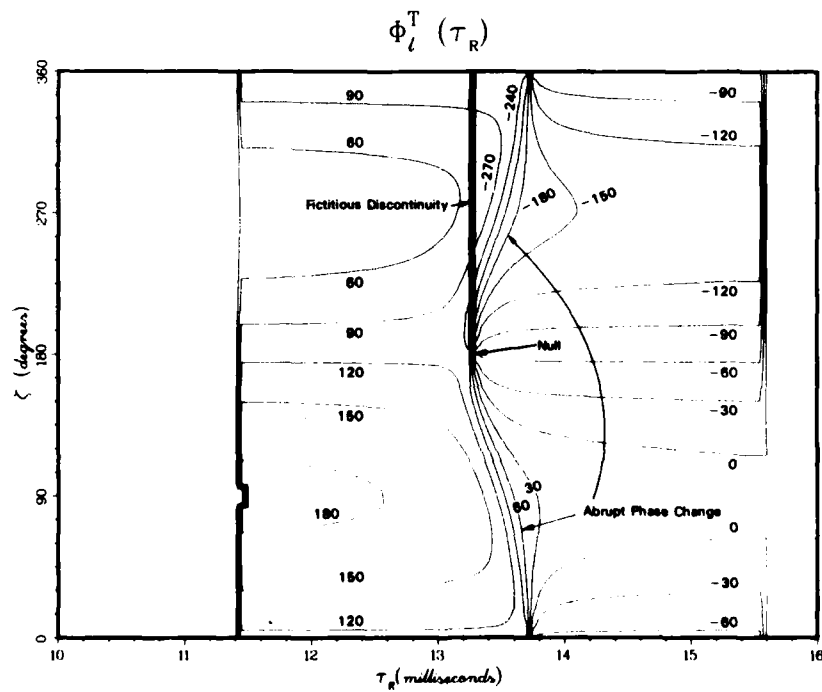


Fig. 35d — Phase behavior corresponding to Fig. 35b

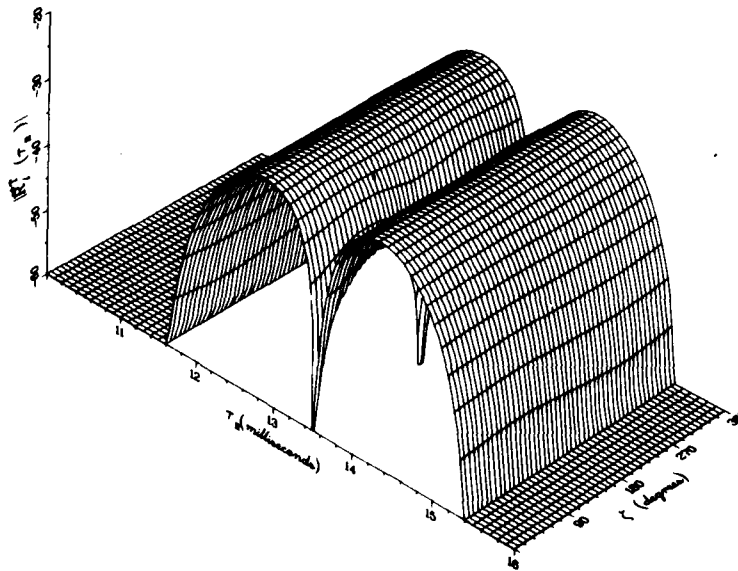


Fig. 36a — Amplitude behavior of $\bar{R}_I^T(r_R)$ for $\gamma = 0^\circ$, calculated with the parameters of Table 2

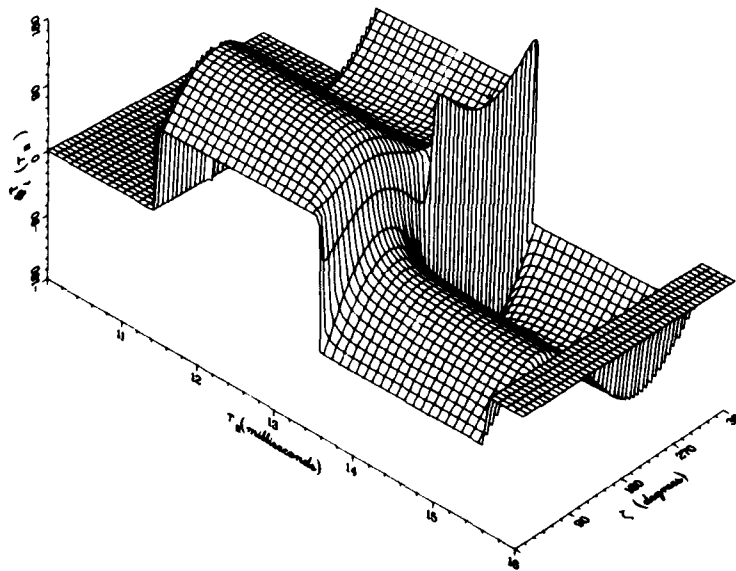


Fig. 36b — Phase behavior of $\bar{R}_I^T(r_R)$ for $\gamma = 0^\circ$, calculated with the parameters of Table 3

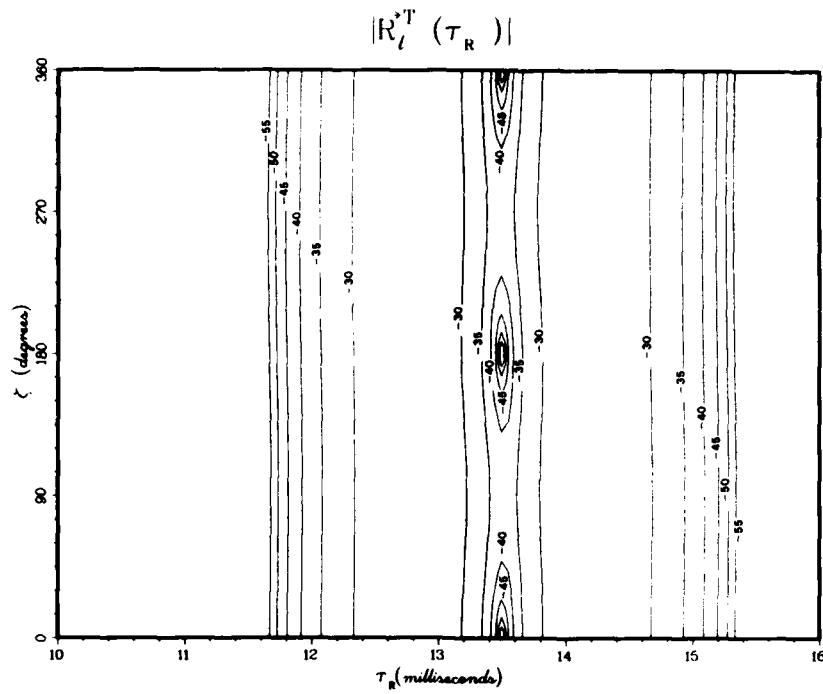


Fig. 36c — Amplitude contours corresponding to Fig. 36a

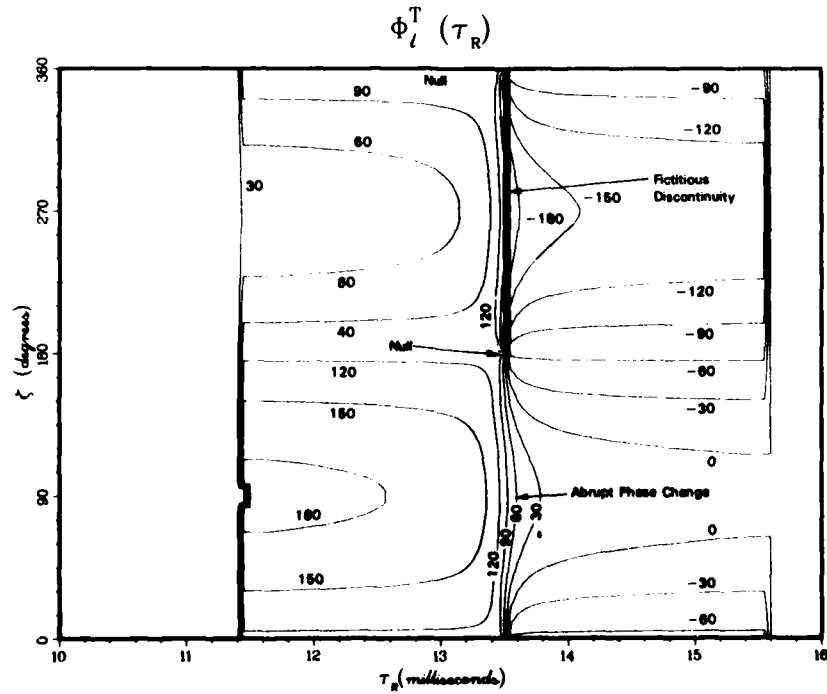


Fig. 36d — Phase behavior corresponding to Fig. 36b

Discussion

Figure 24 shows the correlator performance for the case of a completely horizontal antenna. For this case $|\bar{R}_I(\tau_R)|$ goes to zero at $\zeta = 90^\circ$ and 270° , and there are sudden 180° phase flips at these angles. The best correlation time appears to be at $\tau_R = 13.5$ ms, which is the middle of the correlation peak.

Figure 25 shows the correlator performance for the case of an antenna with inclination $\gamma = 85^\circ$ from the vertical. For this case it is difficult to say if there is a single best receiver synchronization time τ_R . During most of the orbit it appears that the time $\tau_R = 13.5$ ms would be the best. However, this value of τ_R appears to give a value of $|\bar{R}_I^T(\tau_R)|$ that is severely reduced at $\zeta = 90^\circ$ and $\zeta = 270^\circ$. For this case a system of selection of three values of τ_R separated by 1-ms intervals (12.5, 13.5, and 14.5 ms) would give a more stable average performance in the evaluation of $\bar{R}_I^T(\tau_R)$. The discontinuity in Fig. 25d at $\tau_R = 13.8$ ms, signified by the heavy vertical line, is due to a 360° ambiguity which has no real significance except at the nulls ($\zeta = 120^\circ$ and $\zeta = 240^\circ$), where $|\bar{R}_I^T(\tau_R)| \rightarrow 0$. Comparison of Figs. 25c and 25d illustrate this feature clearly.

Figure 26 shows the correlation performance for an antenna with $\gamma = 80^\circ$. In the vicinity of $\tau_R = 14.0$ ms and $\zeta = 180^\circ$ there is an abrupt drop of signal and jump in phase. Otherwise the $|\bar{R}_I(\tau_R)|$ function seems fairly well behaved.

Figure 27 shows the behavior of $\bar{R}_I^T(\tau_R)$ for an antenna with $\gamma = 60^\circ$. The amplitude and phase variation of the correlation are much milder than for the cases with smaller values of γ , since the vertical electric-field components exceed the horizontal components by at least one order of magnitude at this droop angle. This trend is continued as γ is decreased to 45° and then to 0° in Figs. 28 and 29.

Figure 30 gives the value of $\bar{R}_I^{(1)ve}(\tau_R)$. It illustrates the case of pure first-order-mode propagation from a vertical electric-dipole source.

The values of the propagation quantities in Table 3 are similar to those of Table 2 except for an adjustment to produce maximum mode cancellation and interference effects. We have made the first-order and second-order vertically generated modes have opposite phase and equal magnitude. We have modified the phase of the horizontally generated modes so they are in the same phase plane with the vertically generated modes to produce maximum field-strength variation. Hence both severe effects appear in Figs. 31 through 36.

Figure 31 gives the behavior of $\bar{R}_I^T(\tau_R)$ for the propagation parameters of Table 3. The results are almost identical to those of Fig. 24, since $\gamma = 90^\circ$ and the only changes made in the parameters of the horizontally generated modes are to the phase delay times $\tau_{f,hc}$ and $\tau_{f,hc}$.

Figure 32 shows the behavior of $\bar{R}_I^T(\tau_R)$ for the case of $\gamma = 85^\circ$. The influence of the splitting of the vertically generated function is more evident on the phase plot than on the amplitude plot.

Figure 33 shows the behavior of $\bar{R}_I^T(\tau_R)$ for the case of $\gamma = 80^\circ$. Here, the influence of the correlation-peak splitting of the vertically generated function is quite evident as the notch in the correlation peak makes its way from side to side through the values of τ_R and ζ . This is illustrated further in Figs. 34 and 35, which give the graphs for $\gamma = 60^\circ$ and 45° .

Finally, Fig. 36 shows the split correlation peak for a purely vertical antenna being carried around an orbit. Here we find a nearly constant variation of $|\bar{R}_I^T(\tau_R)|$ versus ζ , and the phase of the correlation function $\phi_I^T(\tau_R)$ varies only moderately with ζ . As a function of τ_R , these variables show the expected splitting.

The phase $\phi_I^T(\tau_R)$ changes gradually with τ_R in Figs. 27 through 29, whereas in Figs 34 through 36 it changes abruptly at certain τ_R values but then achieves a constant value again on either side of the change point. This is readily explained using the diagrammatic techniques previously discussed, since in the first case the correlation function for the individual modes $\bar{R}_I^{(1)}(\tau_R)$ are not coplanar, and in the second case they are coplanar, so that only abrupt phase changes are permitted.

CONCLUSIONS

This report shows possible types of variation of the correlation vector $\bar{R}_I^T(\tau_R)$ when an airborne VLF transmitting system is employed. Use of a single correlator-synchronization time can result in loss of communications because of possible signal degradation and phase change caused by orbital and modal interference effects. Multiple and/or adaptive correlation and decision techniques seem indicated for this channel.

REFERENCES

1. F.J. Rhoads and W.E. Garner, "An Investigation of the Modal Interference of VLF Radio Waves," *Radio Science* 2, 539-546 (1967).
2. J.R. Wait and K.P. Spies, "Characteristics of the Earth-Ionosphere Waveguide for VLF Radio Waves," NBS Tech. Note 300, 1964.
3. F.J. Kelly, "VLF Field Strength Variation from an Orbiting Inclined Antenna," *Radio Sci.* 5, 785-791 (1970).
4. J. Galejs, *Terrestrial Propagation of Long Electromagnetic Waves*, Pergamon Press, New York, 1972, p. 331.
5. I.J. Rothmuller, "Effect of the VLF Propagation Channel on Spread-Spectrum Communication Systems", NELC TR 1834, 4 Aug. 1972.
6. F.J. Kelly, "Multimode and Dispersive Distortion in the Very-Low-Frequency Channel," *Radio Sci.* 5, 569-573 (1970).
7. W.J. Judge, "Multiplexing using Quasiorthogonal Binary Functions", *AIEE Trans. Commun. Electron.* 81, 81-83 (1962).

END

DATE
FILMED

1-82

DTIC